Thioether-functionalized cellulose for the fabrication of oxidation-responsive biomaterial coatings and films

Eric M. DuBois[1], Kate E. Herrema[1], Matthew G. Simkulet[1], Laboni F. Hassan[1], Payton R. O'Connor[1,†], Riya Sen[1,‡], and Timothy M. O'Shea[1]*

*corresponding author: toshea@bu.edu

1. Department of Biomedical Engineering, Boston University, Boston, MA, 02215-2407, USA.
† Department of Biomedical Engineering, Rensselaer Polytechnic Institute, Troy, NY, 12180-3590, USA.
‡ Wallace H. Coulter Department of Biomedical Engineering, Georgia Institute of Technology and Emory University, Atlanta, GA, 30332, USA.

Abstract

Biomaterial coatings and films can prevent premature failure and enhance performance of chronically implanted medical devices. However, current hydrophilic polymer coatings and films have significant drawbacks, including swelling and delamination. To address these issues, we modified hydroxyethyl cellulose with thioether groups to generate an oxidation-responsive polymer, HEC_{MTP}. HEC_{MTP} readily dissolves in green solvents and can be fabricated as coatings or films with tunable thicknesses. HEC_{MTP} coatings effectively scavenge hydrogen peroxide, resulting in conversion of thioether groups to sulfoxide groups on the polymer chain. Oxidation-driven, hydrophobic-to-hydrophilic transitions that are isolated to the surface of HEC_{MTP} coatings under physiologically relevant conditions increase wettability, decrease stiffness, and reduce protein adsorption to generate a non-fouling interface with minimal coating delamination or swelling. HEC_{MTP} can be used in diverse optical applications and permits oxidation-responsive, controlled drug release. HEC_{MTP} films are non-resorbable *in vivo* and evoke minimal foreign body responses. These results highlight the versatility of HEC_{MTP} and support its incorporation into chronically implanted medical devices.

Teaser

Modification of cellulose polymer into a non-resorbable, oxidation-responsive biomaterial affords multi-functional coatings and films.

Introduction

Chronically implanted medical devices, such as pacemakers (*1*), catheters (*2*), electrodes (*3*), pumps (*2*, *4*) and prostheses (*5*, *6*), are used widely for monitoring and treating disease. Despite successful clinical implementation, these devices can experience various problems that cause premature device failure (*7–11*). Biomaterials formulated as coatings, which adhere or bond to the device surface, or films, which can be press-fit as a separate material layer onto devices, can prevent premature failure of chronically implanted medical devices as well as enhance their functionality and performance (*12*). Employing hydrogel- and hydrophilic polymer-based coatings or films of polyethylene glycol (PEG) (*13*, *14*), zwitterionic polymers (eg. polycarboxybetaine, polysulfobetaine) (*13*, *15*, *16*), or other synthetic polymers (*17*, *18*) improves long-term medical device performance by altering device surface chemistry, wettability, topography, and/or mechanical properties. Coating- or film-derived surface modifications mitigate molecular and cellular fouling and thrombosis, reduce foreign body response (FBR)-mediated inflammation, and minimize fibrotic encapsulation that would otherwise cause the formation of opaque, cell-dense, fibrotic scar tissue layers around uncoated devices (*12*, *19–22*). Biomaterial coatings and films can also reduce the mechanical stiffness mismatch at the implant-tissue interface to minimize the activation of mechanosensitive receptors (*19*, *20*, *22*), limit friction and wear (*23*, *24*), mitigate damage from device micromotion (*25*), and prevent corrosion and subsequent device degradation (*26*), thereby attenuating pro-inflammatory macrophage states and the fibroblast to myofibroblast transitions that promote capsular contracture. Naturally-derived biomolecules and extracellular matrix (ECM) protein-based coatings and films have also been incorporated as biomimetic substrates on devices to limit immune recognition and enhance device-tissue integration (*27–31*). Aside from regulating FBR and cell interactions, biomaterial coatings and films can be imparted with additional traits to improve long-term device performance including antimicrobial resistance to prevent biofilm formation, controlled local small molecule drug release, and localized gene or viral vector delivery (*12*).

Despite conferring important functions to medical devices, currently available biomaterial coatings and films still have significant drawbacks. Hydrophilic polymer coatings implanted in a dehydrated state can swell greater than 3 times in size *in vivo*, leading to increased compressive tissue damage, increased impedance, coating delamination from the underlying device, and patient discomfort (*32–34*). Coatings and films applied as soft, hydrated polymers can also easily delaminate or shear off during implantation, leading to the exposure of the underlying surface of the implant, which can stimulate deleterious FBRs (*35*). Hydrophilic polymers delaminated from devices also pose an increased embolism risk and can disseminate and deposit at distant tissue sites away from the implant, leading to persistent, non-healing abscesses (*36*). Direct chemical bonding of hydrophilic polymers to the device surface can overcome delamination issues but requires specialized surface preparation that cannot be applied to all devices (*13*, *37*). Natural ECM-based coatings and films suffer from sourcing and scaling issues, as well as increased immunogenic risk (*38–41*). To address these issues, materials engineering approaches are needed to generate new hydrophilic, non-fouling biomaterials that can be stably incorporated onto medical devices, so that they are resistant to disruption during implantation, persist chronically, and do not significantly swell *in vivo*. Additionally, beyond satisfying these general specifications, applications of biomaterial coatings and films could require other context-dependent properties, such as limited light scattering for optical devices, minimal impedance for electrical recording and stimulation, or the ability to elute drugs to direct local biological actions. Cost and manufacturability should also be

considered for the effective scale up and clinical translation of coating and film technologies.

Cellulose-based materials have been used in industrial coating applications dating back to the late 1800's, starting with water repellent, scratch resistant, nitrocellulose-based lacquers (*42*). Due to their natural abundance and renewable sourcing, coatings and films derived from cellulose esters have become ubiquitous in many diverse industrial applications including: dialysis and filtration membranes (regenerated cellulose) (*43*), photography film and coatings on drug formulations to modify release kinetics (cellulose esters, including cellulose acetate and cellulose acetate butyrate) (*44*, *45*), lacquer coatings (cellulose acetate butyrate) (*42*, *46–49*), and tape (cellulose acetate) (*50*). Across all these applications, chemical modification of the hydroxyls on the repeating anhydroglucose unit of cellulose confers emergent and modular properties, including the ability to be dissolved in organic solvents and increased hydrophobicity necessary to repel water (*51–55*). Cellulose-based materials have received only limited use as coatings or films on chronically implanted medical devices because hydrophilic derivatives swell, readily delaminate, and have challenging solubility profiles for fabrication (*53*). Although cellulose esters have improved solubility profiles in organic solvents, which allows them to form effective coatings or films, their poorer surface wettability compared to hydrophilic polymers causes increased protein and cell fouling that impacts overall biocompatibility (*56–58*). New cellulose derivatives that afford the processability of cellulose esters to generate effective coatings and films, while also facilitating the hydrophilic interface necessary for enhanced biocompatibility, would be broadly appealing for use with chronically implanted medical devices.

Here, we derived a new, smart, cellulose-based material that can be readily formulated as a coating or film, persists chronically *in vitro* and *in vivo*, and enables the generation of a soft, non-fouling, hydrophilic interface with minimal material swelling. To achieve this, we leveraged chemistry bioinspired by methionine-based materials (*59*) to endow a specific cellulose polymer, hydroxyethyl cellulose (HEC), with thioether groups and confer oxidation-responsive properties. Upon oxidation under physiologically relevant conditions, this new thioether-functionalized cellulose readily transitions from a hydrophobic to a hydrophilic polymer via the conversion of the pendant thioethers to sulfoxide groups. We hypothesized that a thioether-functionalized, cellulose material would be soluble in organic solvents and thus processable as both coatings or films and that the exposed surface of these preparations would be readily oxidizable *in vivo* by physiological concentrations of reactive oxygen species, leading to the formation of a substrate that is more hydrophilic, non-fouling, and soft, which would confer enhanced biocompatibility. To test this hypothesis, we synthesized the thioether-functionalized cellulose polymer, HEC_{MTP}, at large scales using a robust, single step isothiocyanate-based reaction, and investigated its ability to serve as an effective biomaterial coating and film. HEC_{MTP} readily dissolves in organic solvent systems, and coating outcomes, such as thickness and surface roughness, could be tuned by adjusting composition and fabrication parameters. Treatment of HEC_{MTP}-coated substrates with physiological concentrations of hydrogen peroxide *in vitro* resulted in selective oxidation of thioether groups that served to increase surface hydrophilicity, decrease the effective surface mechanical stiffness, and reduce the extent of protein adsorption and neural cell fouling while causing negligible material swelling. We demonstrated the utility of HEC_{MTP} coatings for optical applications and HEC_{MTP} films for oxidation-responsive controlled release of molecules. HEC_{MTP} films persist *in vivo* for at least 4 weeks when implanted subcutaneously and show minimal

immune cell recruitment and fibrotic scarring compared to equivalent non-oxidation responsive cellulose biomaterials. Our findings demonstrate the feasibility of using this oxidation-responsive, thioether-functionalized cellulose platform to improve the function and longevity of chronically implanted medical devices.

Results

Thioether-functionalized cellulose (HEC_{MTP}) is an oxidation-responsive polymer

We selected hydroxyethyl cellulose (HEC) as a template cellulose polymer for post-polymerization modification with thioether groups as it is highly abundant, inexpensive, has been previously used in medical applications, and is commercially available in numerous molecular weights. HEC contains accessible primary hydroxyls on the repeating anhydroglucose unit that can be used as nucleophilic species in isothiocyanate- and isocyanate-based reactions. HEC (380 kDa) was reacted with excess 3-(methylthio)propyl isothiocyanate in dimethyl sulfoxide (DMSO) with n,n-diisopropyl ethylamine (DIEA) as a catalyst to generate a new polymer, HEC_{MTP}, which has 3-(methylthio)propyl (MTP) groups attached to the HEC polymer backbone by a stable thiocarbamoyl linker (**Fig. 1A, Table S1**). HEC_{MTP} could be prepared with 5-23 mol% MTP functionalization relative to the available free primary hydroxyls, with moderate control of functionalization achieved through tuning reaction stoichiometry (**Fig. 1B-C, Fig. S1**). While HEC readily dissolved in water to form a viscous solution, HEC_{MTP} at functionalities as low as 9 mol% formed hydrated gels, and at functionalities greater than 15 mol% was insoluble in water (**Fig. 1D, S1**). Based on an initial screen of different functionalizations, HEC_{MTP} with MTP functionalization at an average of 21 mol%, or ~0.63 MTP groups per estimated anhydroglucose unit repeat, was selected for detailed evaluation. All studies reported here were completed using a single batch of HEC_{MTP} that was derived by blending the yields from 4 individual, 1 gram-scale reactions of near equivalent functionality (**Table S2, Fig. S2B**).

To determine whether thioether groups on HEC_{MTP} could be oxidized to generate the sulfoxide-functionalized polymer, designated as HEC_{SO}, we exposed HEC_{MTP} to oxidizing conditions for one day using 1% (327mM) hydrogen peroxide (H_2O_2) (**Fig. 1E**). Conversion of thioether groups to sulfoxide groups was detected by ^1H NMR as a readily identifiable shift in the thioether methyl protons from 2.15 ppm to 2.92 ppm (**Fig. 1F**) (*60*). Using 1% H_2O_2, all thioether groups were converted to sulfoxide groups, verified by complete loss of the thioether methyl protons at 2.15 ppm (**Fig. 1F, S2**). By FTIR, HEC_{MTP} showed emergent -CS-NH- and -O-CS- (thiocarbamoyl) stretches at 1535 cm^{-1} and 1710 cm^{-1} respectively following MTP addition (*61*, *62*), while oxidation of HEC_{MTP} to HEC_{SO} showed characteristic emergence of a S=O stretch at 1055 cm^{-1} (**Fig. 1G**) (*63*). Under the 1% H_2O_2 oxidation conditions, the FTIR spectra within the thiocarbamoyl region showed a notable increase in the intensity of the 1710 cm^{-1} stretch and a concurrent reduction in the 1535 cm^{-1} stretch which is consistent with the sulfur atom in the thiocarbamoyl being substituted by an oxygen atom to form -O-CO-NH- (**Fig. 1G**) (*61*). Despite these changes, there was preserved total integration of the two stretches within the thiocarbamoyl region (**Fig. S3A-B**).

Following oxidation, there was a reduction in the total integrated area of methyl protons by NMR in HEC_{SO} samples compared to unmodified HEC_{MTP}. We suspected that the attenuated total detected sulfoxide-associated methyl protons on HEC_{SO} by NMR was a result of significantly reduced solubility in dTFA (deuterated trifluoroacetic acid) as well as other common NMR solvents, whereas HEC and HEC_{MTP} dissolved completely in

dTFA and returned clean NMR spectra. Oxidizing HEC_{MTP} with lower concentrations of H_2O_2 within the physiological range (80-320μM) for one day resulted in partial oxidation of the polymer, such that it was still completely soluble in dTFA for NMR evaluation. Under these dilute oxidizing conditions, we detected partial conversion of thioether groups to sulfoxides and preservation of methyl protons by NMR, implying no cleavage of functionalized groups from the HEC backbone (**Fig. S3C**). Evaluation of HEC_{MTP} samples before and after oxidation by X-ray photoelectron spectroscopy (XPS) also corroborated the preservation of sulfur content on the polymer after oxidation (**Fig S4**). We did not detect any notable changes to stretches in the thiocarbamoyl region by FTIR in these samples implying preferential thioether oxidation over thiocarbamoyl oxidation upon exposure to physiological concentrations of H_2O_2 (**Fig S5**). The template polymer, HEC, was not altered following one day of 1% H_2O_2 exposure, which indicated that there was no detectable oxidation of ethylene oxide groups on the polymer backbone to which MTP groups were linked (**Fig. S6**). Collectively, these data demonstrate that there was negligible cleavage of the MTP group from the HEC polymer backbone after oxidation and preferential oxidation of the thioether moiety, consistent with previous reports using similar chemistries (*64*, *65*). Characterization of HEC_{MTP} by differential scanning calorimetry (DSC) and thermal gravimetric analysis (TGA) showed that HEC_{MTP} was thermally stable up to 215°C, making it amenable to a wide range of processing conditions and methods (**Fig. S7**).

To assess differences in wettability between HEC variants, we performed sessile-drop goniometry on casted films of HEC, HEC_{MTP}, and HEC_{SO} to evaluate relative hydrophilic-hydrophobic character. As anticipated, MTP functionalization resulted in a significant decrease in wettability, with HEC_{MTP} displaying a contact angle of 67° which was more than double that of the unmodified HEC (24°) and within the range of reported values for other cellulose ester benchmarks (**Fig. 1H**) (*66*). Oxidation of HEC_{MTP} to HEC_{SO} yielded a significant 48° decrease in contact angle, resulting in a surface that had equivalent wettability to HEC, demonstrating that oxidation with 1% H_2O_2 is an effective chemical stimulus to substantially increase the hydrophilicity of this thioether-functionalized cellulose by converting thioether functional groups to sulfoxides (**Fig. 1H**).

Collectively, these data show that HEC can be readily modified with thioether functionalities at high scale and with stoichiometric control to generate a new, oxidation responsive polymer, HEC_{MTP}. Oxidation of HEC_{MTP} prompted sulfoxide conversion but no pendant group cleavage and was sufficient to transition HEC_{MTP} from a water insoluble polymer to a hydrophilic polymer. Since HEC_{MTP} possessed the unique capacity to be processed using organic solvents like a cellulose ester but also to selectively transition into a hydrophilic interface via a ubiquitous biological stimulus, we were prompted to explore in earnest its potential as a coating and film for biomedical applications.

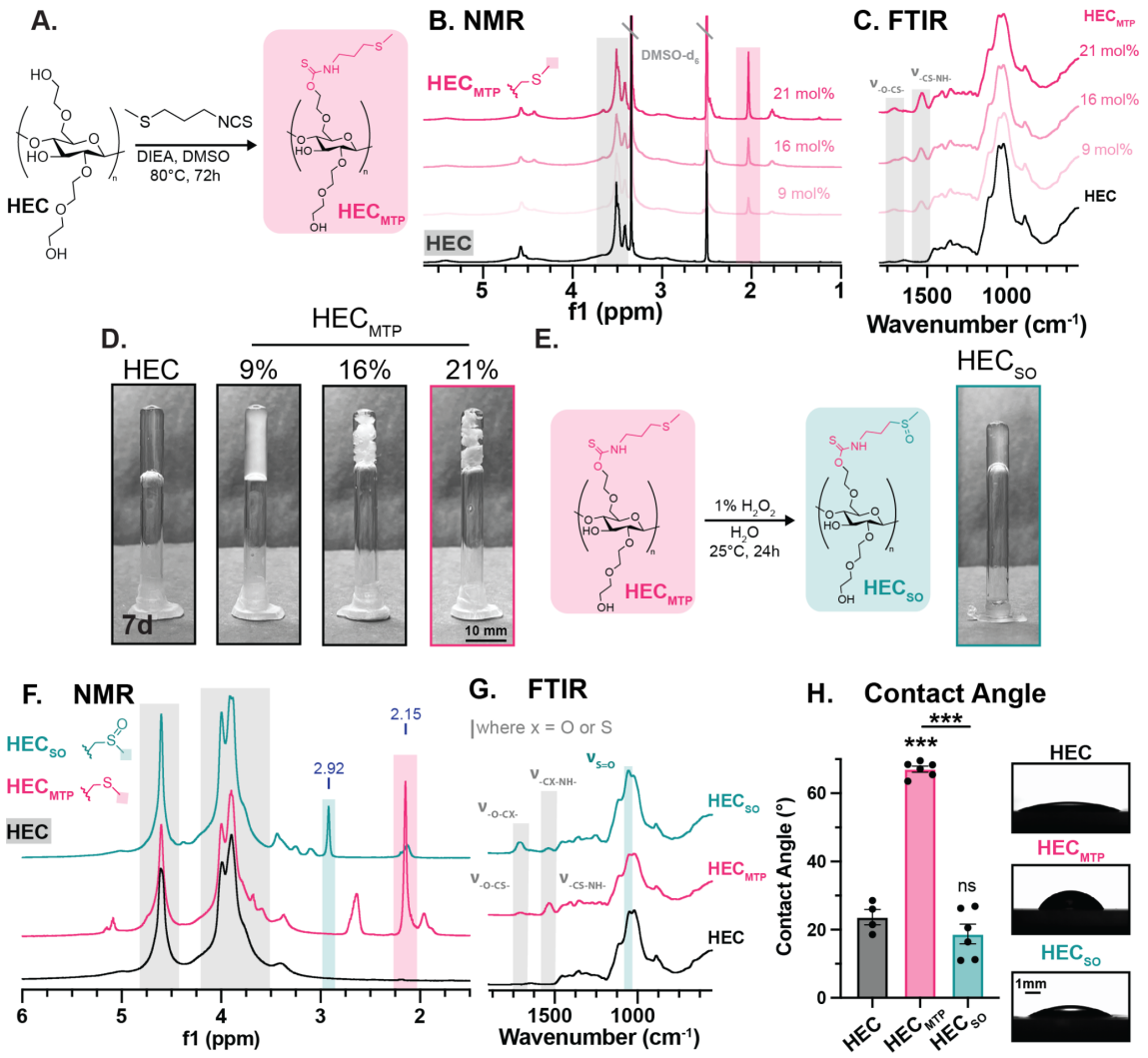

Fig. 1: Characterization of HEC$_{MTP}$ polymers demonstrates control of physicochemical properties. (A) Synthesis scheme for base-catalyzed, nucleophilic addition of MTPI to HEC to form HEC$_{MTP}$. **(B)** ^{1}H NMR of HEC and HEC$_{MTP}$ at 9, 16, and 21mol% functionality in dDMSO. **(C)** FTIR of HEC and HEC$_{MTP}$ at 9, 16, and 21mol% functionality highlighting MTP-associated peaks. **(D)** HEC and HEC$_{MTP}$ at 9, 16, and 21mol% solubilized at 5wt% in PBS. **(E)** HEC$_{MTP}$ can be oxidized to form HEC$_{SO}$ via the application of 1% H_2O_2 in water for 24hr. Resulting HEC$_{SO}$ solubilized at 5wt% in PBS. **(F)** ^{1}H NMR in dTFA highlighting characteristic peaks associated with HEC, HEC$_{MTP}$ and HEC$_{SO}$. Labels in blue demarcate peak location. **(G)** FTIR with characteristic absorption bands of chemical bonds in HEC, HEC$_{MTP}$ and HEC$_{SO}$. **(H)** Contact angle data demonstrating a significant increase in hydrophobicity on the addition of the thioether moiety to HEC, and a subsequent, significant decrease in hydrophobicity upon oxidation of the thioether moiety (HEC$_{SO}$). Inset: brightfield images from the goniometer demonstrating the deposition of deionized (DI) water on HEC, HEC$_{MTP}$ and HEC$_{SO}$ films. Not significant (ns) and ***$P < 0.0001$ compared to HEC or as designated, one-way ANOVA with Tukey's multiple comparison test. Graph shows mean ± s.e.m. with individual data points showing n = 4 for HEC, n = 6 for HEC$_{MTP}$ and HEC$_{SO}$.

HEC_{MTP} can be fabricated as a coating or film

Dip coating is a standard industrial technique for processing coatings of cellulose esters with coating properties, including thickness and surface finish, readily altered by key formulation parameters such as solvent system and temperature (*67–69*). To determine an appropriate solvent system in which HEC_{MTP} could be solubilized for coating applications, we prepared HEC_{MTP} at 10mg/mL in common green organic solvents including DMSO, methanol, ethanol, isopropyl alcohol (IPA), acetone, and water. At this relatively dilute concentration, HEC_{MTP} was soluble in DMSO but was insoluble, and did not disperse, in any of the other solvents (**Fig. 2A**). To identify a wider range of useful solvent systems for preparing HEC_{MTP}, we generated and tested blends of DMSO with the same array of green organic solvents at 50%/50% v/v composition. HEC_{MTP} was soluble in all DMSO blended solvent systems except for DMSO/water in which an insoluble, dispersed polymer phase was noted (**Fig. 2B**).

Viscosity of cellulose solutions influences the thickness and regularity of finished coatings, as well as its workability during processing (*67–69*). Therefore, we next used rheological testing to assess the effect of solvent system, polymer concentration, and temperature on the viscosity of HEC_{MTP} solutions. The composition of DMSO/organic solvent blends impacted HEC_{MTP} solution viscosity, with increasing proportions of acetone in a DMSO/acetone blend resulting in a dramatic increase in the viscosity of 5wt% HEC_{MTP} solutions, ranging from 15.1 Pa.s at 0% acetone to 119.8 Pa.s with 50% acetone incorporation (**Fig. 2C**). Increasing the concentration of HEC_{MTP} in DMSO-only formulations from 1wt% to 3wt% also caused a significant increase in viscosity from 0.09 to 1.6 Pa.s, while the viscosity of 5wt% preparations increased by an order of magnitude to 15.1 Pa.s (**Fig. 2D**). There was a notable effect of temperature on HEC_{MTP} solution viscosity and we observed a significant, linear decrease in viscosity from 10 Pa.s at 30°C to 2.0 Pa.s at 70°C (**Fig. S8A-B**). Taken together, these data suggest that HEC_{MTP} solution viscosity can be readily tuned across 3 orders of magnitude by adjusting polymer concentration, solvent system, and temperature at processing.

We next tested how HEC_{MTP} solution viscosity influences the thickness and roughness of prepared coatings. We used acid-cleaned glass slides and dipped HEC_{MTP} solutions at a fixed rate of 1 mm/sec (the fastest rate that still approximately maintains zero-shear viscosity or a shear rate of 1 sec^{-1}) and allowed slides to dry in a vacuum oven at 40°C for at least 72 hours to remove residual DMSO solvent and form the coating (**Fig. 2E**). We identified differences in the thickness of HEC_{MTP} coatings prepared from different DMSO/acetone blends at 5wt% HEC_{MTP} with all formulations resulting in coatings with a thickness ranging from 10-25µm (**Fig. 2F, S8C-D**). There was a notable change in surface roughness due to solvent blending, with 50% DMSO/acetone solutions demonstrating large, undulating surface roughness on the micron scale and a significantly higher average roughness (~29.6nm) that was more than double that of the 100% DMSO solvent system (12.7nm) (**Fig. S9A, S9D**). To test the effect of polymer solution concentration on coating thickness and roughness, we prepared dip coated slides at 1, 3, and 5wt% in DMSO only. Increasing the solution's polymer concentration significantly increased the coating thickness from 1.9µm at 1wt% to 14.1 µm at 3wt%, but there was minimal increase in coating thickness between the 3wt% and 5wt% preparations (**Fig. S8D**). Surface profilometry of these coatings revealed that there was a large increase in roughness from 1wt% to 3wt%, but an apparent smoothing at 5wt% (**Fig. S9B, S9E**), suggesting that the higher wt% coating may deposit a significantly greater total amount of HEC_{MTP}, effectively creating a smoother and more uniform coating. When comparing all

the different formulations together, HEC_{MTP} coating thickness was directly proportional to the measured magnitude of viscosity of the coating solution irrespective of solvent system or concentration (**Fig. 2F**). We also evaluated the effects of fabricating multilayer coatings by dipping a substrate in a solution of 5wt% HEC_{MTP} in DMSO and incorporating a 24 hour drying step between subsequent dips. Increasing from 1 to 3 dips resulted in a significant increase in coating thickness from 12.6 to 26.4µm (**Fig. 2G**). Evaluating the average roughness, we observed a small, but significant increase from 1 dip at 12.7nm to 3 dips at 34.3nm (**Fig. 2H, S9C, S9F**).

To form free-standing films from HEC_{MTP}, we first fabricated a silicone mold composed of two, press-fit silicone sheets (**Fig. 2I)**. HEC_{MTP} in DMSO was pipetted to fill the silicone mold cavity and dried in a vacuum oven at 40°C to form a large free-standing film. Individual wafers of defined geometries could be punched out from larger film preparations using a biopsy punch, enabling a rapid and scalable approach to film fabrication (**Fig. 2I**). By depositing a layer of HEC_{MTP} solution every 24 to 48 hours we could tune film thickness from 6.8µm (1 layer) to 66.6 µm (3 layers) with no evidence of lamination defects within multilayered constructs (**Fig. 2J**). These data show that HEC_{MTP} can be dissolved in green organic solvents and processed to form coatings and films whose thickness and roughness can be readily tuned through careful selection of solvent and processing parameters.

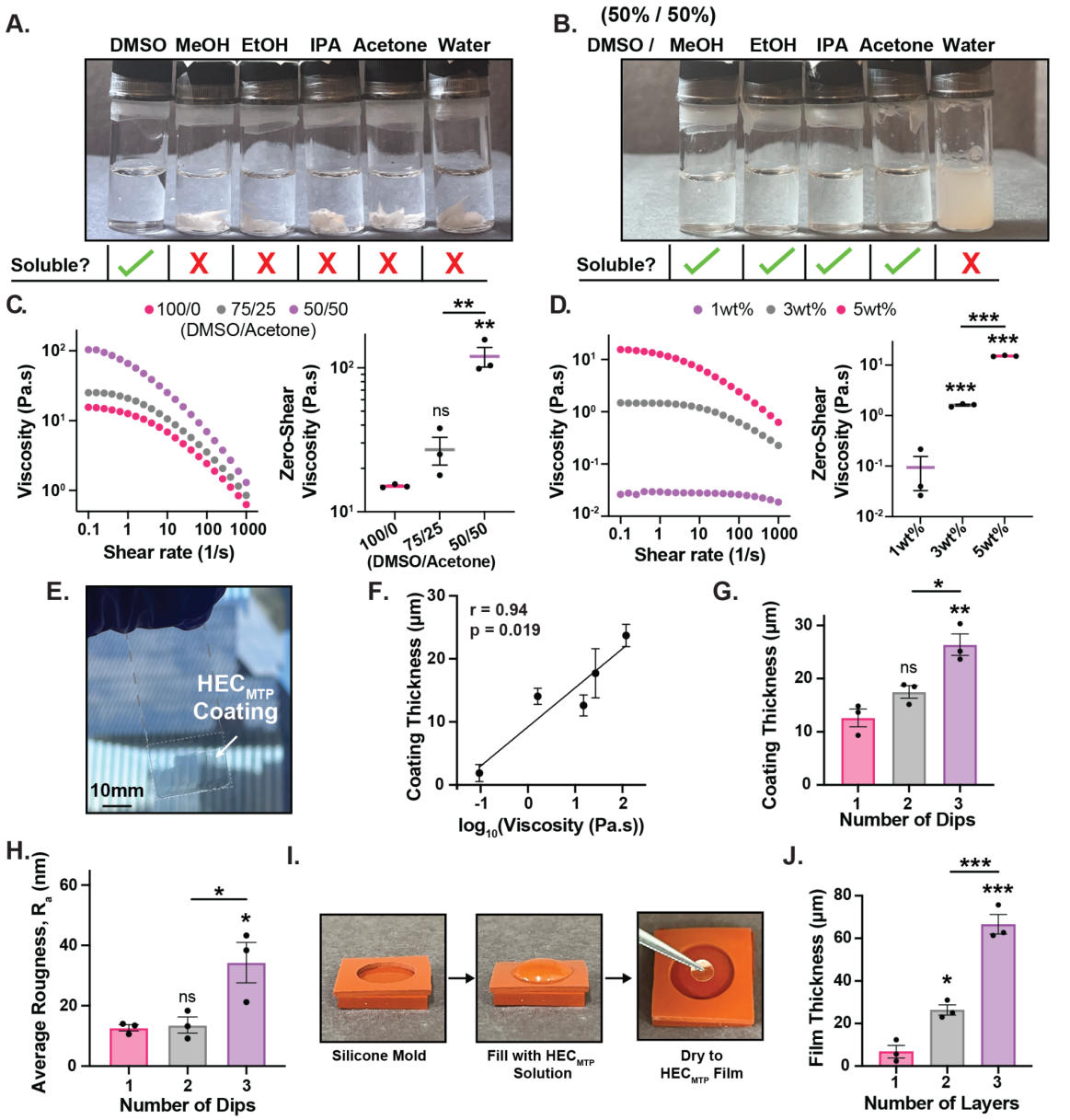

Fig. 2: HEC_{MTP} polymer can be formulated as coatings or films with tunable thickness. (A) Solubility table showing images of HEC_{MTP} polymer solubilized at 10mg/mL in DMSO and insoluble in MeOH, EtOH, IPA, acetone and water. **(B)** Solubility table showing images of HEC_{MTP} polymer solubilized at 10mg/mL in a 50%/50% solvent system of DMSO and MeOH, EtOH, IPA, or acetone, but precipitated in DMSO/water (50%/50%). **(C)** *Left:* Dynamic rheological shear rate sweep measurements for HEC_{MTP} solubilized at 5wt% in a 100/0, 75/25, 50/50 DMSO/acetone solvent system showing viscosity (Pa.s) against increasing shear rate (s^{-1}). *Right:* Box-and-whisker plot showing the increase in zero-shear viscosity (Pa.s), measured at a shear rate of 0.1 (s^{-1}), with increasing concentration of acetone. Not significant (ns) and $^{**}P < 0.003$ compared to 100/0 DMSO/Acetone or as designated. **(D)** *Left:* Dynamic rheological shear rate sweep measurements for HEC_{MTP} at 1, 3, and 5wt% in DMSO showing viscosity (Pa.s) against increasing shear rate (s^{-1}). *Right:* Box-and-whisker plot showing the increase in zero-shear viscosity (Pa.s), measured at a shear rate of 0.1 (s^{-1}), with increasing concentration. $^{***}P \leq 0.001$ compared to 1wt% or as designated. **(E)** Brightfield image showing a HEC_{MTP} coating on a glass substrate. Black dashed lines

outline the glass slide. White dashed lines outline the HEC_{MTP}-coated portion of the glass slide. **(F)** Semi-log scatter plot showing the relationship between viscosity and coating thickness. Graph shows mean viscosity vs. mean coating thickness ± s.e.m. with individual data points showing n = 3 per group. The semi-log data line is fit with a linear line of best fit and the correlation is reported as Pearson's Correlation Coefficient (r). **(G)** Bar graph showing effect of multiple dips of HEC_{MTP} solubilized at 5wt% in 100/0 DMSO/Acetone on coating thickness. *P < 0.03, **P <0.003, and not significant (ns) compared to 1 dip or as designated. **(H)** Bar graph showing the effect of multiple dips on the average roughness of the coating. *P < 0.04, and not significant (ns) compared to 1 dip or as designated. **(I)** Brightfield images showing the film-making process, including: the silicone mold, deposition of soluble HEC_{MTP}, and the resulting dried and punched HEC_{MTP} film. **(J)** Bar graph showing effect of multiple layers on film thickness using a 3wt% HEC_{MTP} solution in DMSO. *P < 0.02, ***P <0.0005 compared to 1 layer or as designated. All statistical comparisons were made using one-way ANOVAs with Tukey's multiple comparison tests. Graphs show mean ± s.e.m. with individual data points showing n = 3 per group.

HEC_{MTP} coatings are oxidation-responsive and stable under simulated physiological conditions

Next, we evaluated the physical and oxidation-responsive properties of HEC_{MTP} when formulated as a coating. To elucidate structure-function correlates for HEC_{MTP} coatings, we synthesized two other HEC derivatives to serve as benchmarking controls: (i) HEC_{HEX}, which contains a thiocarbamoyl linked aliphatic hexyl group of similar length to that on HEC_{MTP} but without the thioether functionality, and (ii) HEC_{OCT}, which contains an aliphatic octyl group linked to the polymer backbone by a carbamate linker (**Fig. S10-11, Table S3-4**). HEC_{HEX} and HEC_{OCT} were appropriate functional controls for evaluating the physical and oxidation-responsive properties of HEC_{MTP} as they were synthesized via equivalent chemistries (isothiocyanate and isocyanate reactions respectively), had similar hydrophobicity to the MTP group, and both lacked thioether functionality. However, important limitations with the fabrication of HEC_{HEX} and HEC_{OCT} benchmarking controls warrant brief review here. Due to the limited reactivity of hexyl isothiocyanate, HEC_{HEX} could only be functionalized to approximately 5 mol% hexyl groups on the polymer chain, which was considerably less than the 21 mol% functionalization that could be readily achieved for HEC_{MTP}. HEC_{OCT}, by virtue of employing more reactive isocyanate rather than isothiocyanate chemistries in its synthesis, could be readily tuned up to 100 mol% functionality. However, at functionalities of 12 mol% and higher, we observed issues with HEC_{OCT} solubility whereby the polymer would either be insoluble in DMSO or would solubilize with mild heating but rapidly crystallize as it cooled (**Fig. S12**). In an attempt to address this issue, we tested 18mol% HEC_{OCT} in a variety of different solvent formulations, including: water, acetone, toluene, and 50/50 DMSO/toluene (**Fig. S13**). HEC_{OCT} at 18 mol% octyl functionalization formed swollen hydrogels in water, was insoluble in acetone and toluene, and was only partially soluble in 50/50 DMSO/toluene, preventing its effective formulation as a free-standing film or coatings. Therefore, with consideration of the above limitations, HEC_{HEX} at 5 mol% hexyl and HEC_{OCT} at 8 mol% octyl groups were used to fabricate coatings for comparisons with HEC_{MTP} coatings.

As a first test of the oxidation-responsive properties of HEC_{MTP} coatings, we drop-casted HEC_{MTP} and benchmarking polymers into wells of a 96 well plate to form thin

coatings that were incubated overnight in 100µL of 4mM hydrogen peroxide at 37°C, which equated to an approximate 2:1 molar ratio of MTP moieties to H_2O_2. At 24 hours, HEC_{MTP} coatings had scavenged 82.8% (or 1046.5 µmol/cm^2) of the available H_2O_2 whereas HEC and HEC_{OCT} coatings did not scavenge any detectable amount of H_2O_2 (**Fig. 3A**). HEC_{HEX} scavenged a small but significant amount of incubated H_2O_2 (15.6%), likely through oxidation of the thiocarbamoyl linker as noted earlier (**Fig. 3A**). FTIR-based comparisons of HEC, HEC_{HEX}, HEC_{OCT} , and HEC_{MTP} before and after oxidation with 1% H_2O_2 confirmed that both HEC_{HEX} and HEC_{MTP} had H_2O_2-induced changes in the two stretches in the thiocarbamoyl region consistent with the sulfur atom on the thiocarbamoyl being substituted for by an oxygen atom (*61*) (**Fig. S14**). HEC and HEC_{OCT} showed no apparent change in their respective FTIR spectra after oxidation which further strengthened our confidence in the assessment that the thiocarbamoyl was altered in the HEC_{HEX} and HEC_{MTP} polymers under these millimolar-range H_2O_2 conditions.

To profile the kinetics of HEC_{MTP} oxidation we assessed the amount of H_2O_2 scavenged at defined time points from 1 hour to 7 days (**Fig. 3B**). H_2O_2 scavenging by HEC_{MTP} demonstrated second order rate kinetics resulting in a sigmoidal time dependency, which was consistent with an autocatalytic process that has previously been observed in polysulfide-based materials (*70*) (**Fig. S15A**), with nearly all H_2O_2 (>99%) consumed following one week of incubation. HEC_{MTP} coatings scavenged H_2O_2 in a concentration dependent manner which was directly proportional to the initial concentration of applied H_2O_2 within the concentration range of 80µM to 8mM (**Fig. 3C**). To further dissect the concentration and load dependent effects, we exposed HEC_{MTP} coatings to either 100µL of H_2O_2 at 4mM or 200µL of H_2O_2 at 2mM to evaluate different concentrations but conserved total molar equivalents of H_2O_2. After 24 hours, the HEC_{MTP} coatings had scavenged 82% of the 4mM H_2O_2 but only 55% of the 2mM H_2O_2, demonstrating the strong dependency of H_2O_2 concentration on the scavenging rate of the film (**Fig. S15B**). We also noted a finite H_2O_2 scavenging capacity for HEC_{MTP} coatings that affected scavenging kinetics, such that high initial H_2O_2 loads (8mM) reduced the effective scavenging rate of the coating upon subsequent exposure to a second 4mM H_2O_2 solution (**Fig. S15C**). By contrast, HEC_{MTP} coatings exposed to a 100-fold lower initial H_2O_2 load (80µM) could more effectively scavenge the 4mM H_2O_2 solution upon subsequent exposure (**Fig. S15C**).

At sites of tissue injury and cell death *in vivo*, reactive oxygen species (ROS) are generated at concentrations ranging from 1-100µM, with exposure to 80-100µM ROS capable of causing oxidative stress-mediated cell necrosis or apoptosis (*71*, *72*). We assessed how H_2O_2 scavenging by HEC_{MTP} coatings within such physiological ROS concentrations altered the surface wettability of the coating. Exposing HEC_{MTP} coatings to H_2O_2 concentrations at or greater than 40µM for one day, caused a significant decrease in contact angle with 320µM H_2O_2 incubation resulting in contact angles indistinguishable from HEC_{SO}, which defined the maximum wettability of the surface (**Fig. 3D**). To assess whether the maximum wettability of the surface could be achieved by prolonged exposure to lower, physiologically relevant concentrations of H_2O_2, we incubated HEC_{MTP} coatings in 80µM H_2O_2 for 7 days. Under these milder oxidizing conditions, HEC_{MTP} coatings gradually transitioned to be maximally wettable over the course of 7 days with the greatest rate of change occurring from 1 to 3 days of incubation (**Fig. 3E**). HEC_{MTP} incubated in PBS only showed a small change in contact angle over the 7 day incubation period indicative of a low amount of hydration of the polymer coating, but such effects on surface wettability paled in comparison to those induced by the oxidizing conditions (**Fig.**

3E). Contact angle measurements were paired with bulk physical evaluations including coating swelling and dry mass loss (**Fig. 3F-G, S16**). The wet mass of HEC_{MTP} coatings changed minimally over the course of 7 days when incubated in PBS only, while the gradual hydrophobic to hydrophilic surface transition provoked by oxidation with 80μM H_2O_2 caused a concurrent increase in coating wet mass that reached 67.7% by 7 days (**Fig. 3F, S16**). This change in material wet mass was small and insignificant when compared to the HEC_{HEX} and HEC_{OCT} coatings, which swelled considerably with an increase in wet mass of over 4400% and 2700% respectively (**Fig. 3F**). Over the course of 7 days, HEC_{HEX} coatings slowly dissolved, while HEC_{OCT} coatings delaminated and fragmented, resulting in both coatings subsequently decreasing in both wet and dry mass (**Fig. 3F-G**). By contrast, HEC_{MTP} coatings persisted with minimal polymer resorption over the 7 days, with incubation in either PBS or 80μM H_2O_2 resulting in less than 12% total dry mass loss (**Fig. 3G**). We hypothesized that the persistence and minimal swelling of HEC_{MTP} coatings could be due to strong physical bonding between polymer chains, which is characteristic of certain cellulose ester formulations (*73*). Reexamining the FTIR for HEC_{MTP}, we noted a prominent shoulder in the spectra within the 3200-3300 cm^{-1} region which can be attributed to enhanced intermolecular hydrogen bonding (**Fig. 3H**) (*73*, *74*). This hydrogen bonding phenomena was present only in HEC_{MTP} and was not identified in HEC, HEC_{SO}, or any of the other benchmarking materials. To confirm the presence of intermolecular hydrogen bonding, we assessed whether we could re-dissolve dried HEC_{MTP} films in 1,1,1,3,3,3-hexafluoro-2-propanol (HFIP), a known hydrogen bond disrupting solvent (*75*, *76*). While HEC_{MTP} films swell to nearly 4000% of their original dry mass (but do not dissolve) after 48 hours of incubation in DMSO, HFIP effectively dissolved films in their entirety over the same time course, confirming the presence of strong hydrogen bonding within the dry HEC_{MTP} material (**Fig. S17**).

These data show that HEC_{MTP}, when formulated as a coating, readily scavenges physiologically relevant concentrations of H_2O_2 with second order reaction kinetics that are dependent on both the H_2O_2 and thioether concentrations. Oxidation of HEC_{MTP} coatings under physiologically relevant conditions achieves the maximal wettability of the surface over the course of several days and is associated with a small increase in wet mass as the coating hydrates. Despite hydration at the coating surface, strong intermolecular hydrogen bonding between polymer chains comprising the bulk of the HEC_{MTP} coating results in minimal total swelling and negligible mass loss to ensure long-term preservation of coating integrity.

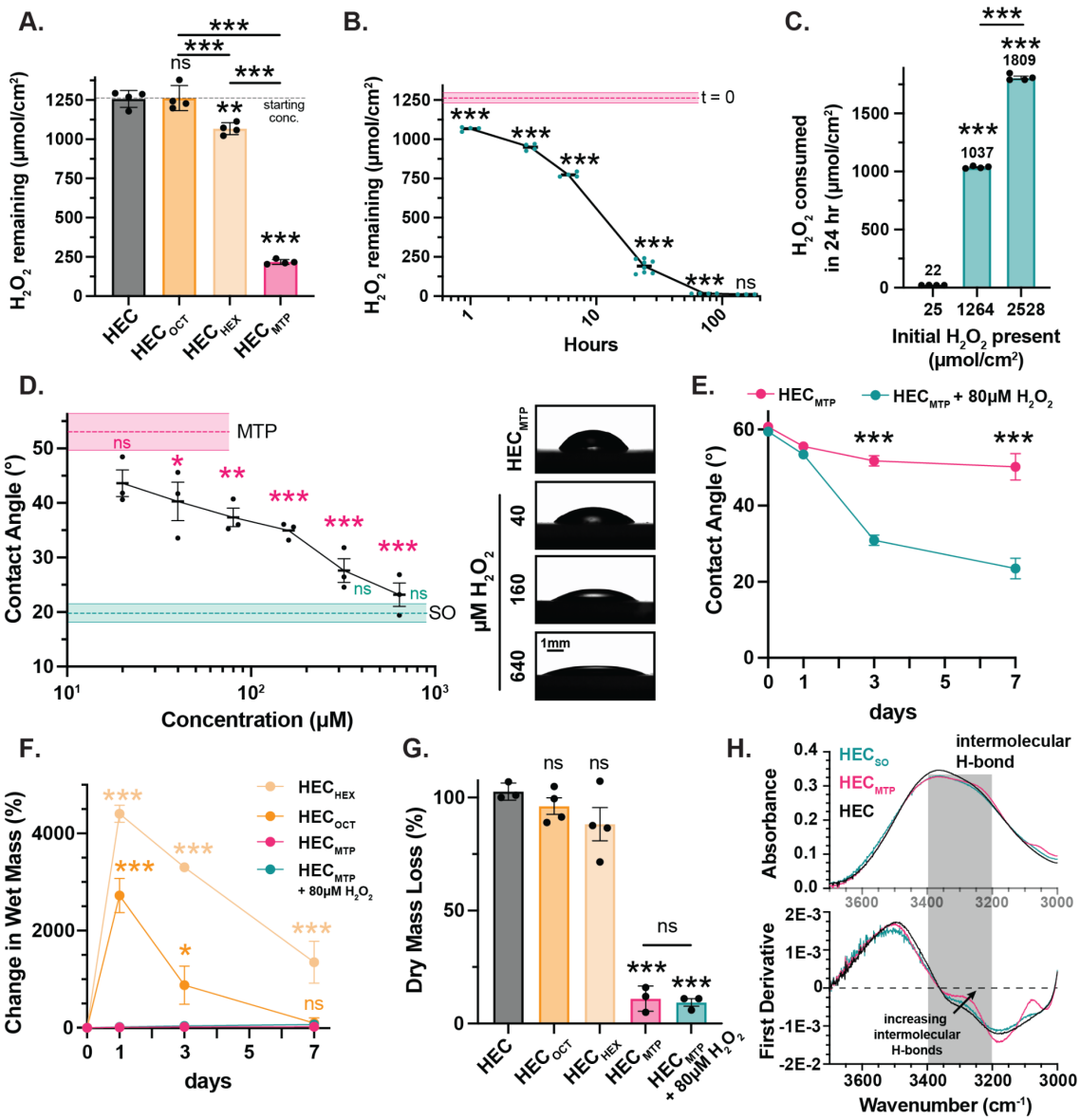

Fig. 3: HEC_{MTP} coatings oxidize in response to H_2O_2 exposure, but are impervious to dissolution in aqueous buffers. (A) H_2O_2 remaining (µmol/cm^2) following exposure of HEC, HEC_{OCT}, HEC_{HEX}, and HEC_{MTP} coatings to 4mM H_2O_2 for 1d. **P <0.0015, ***P ≤ 0.001, and not significant (ns) compared to HEC or as designated, one-way ANOVA with Tukey's multiple comparison test. Graph shows mean ± s.e.m. with individual data points showing n = 4 per group. **(B)** H_2O_2 remaining (µmol/cm^2) after exposure of HEC_{MTP} coating to 4mM H_2O_2 for 1-168 hours (7d). ***P≤ 0.0007, each timepoint is compared with the previous timepoint, one-way ANOVA with Tukey's multiple comparison test. Graph shows mean ± s.e.m. with individual data points showing n = 8 for 24hrs, and n = 4 for all other groups. The line for t = 0 shows mean ± s.e.m., with s.e.m. represented as light shaded areas. **(C)** µmol/cm^2 H_2O_2 consumed after exposure of HEC_{MTP} coatings to 100µL of H_2O_2 at variable concentrations for 1d. ***P< 0.0001 compared to 25 µmol/cm^2 H_2O_2 or as designated, one-way ANOVA with Tukey's multiple comparison test. Graph shows mean ± s.e.m. with individual data points showing n = 4 per group. **(D)** Exposure to increasing concentrations of H_2O_2 for 24 hrs leads to significant decreases in contact angle. *P < 0.03, **P ≤0.004, ***P <0.001, and not significant (ns) with comparisons in pink

being made to HEC_{MTP} (MTP) and comparisons in turquoise being made to HEC_{SO} (SO), one-way ANOVA with Tukey's multiple comparison test. Graph shows mean ± s.e.m. with individual data points showing n = 6 for SO and n = 3 per group for all other conditions. Inset: brightfield images from the goniometer demonstrating the deposition of deionized water on HEC_{MTP} and HEC_{MTP} coatings treated with 40, 160, and 640μM of H_2O_2. **(E)** Contact angle measurements on HEC_{MTP} coatings over 7d exposed to either PBS or PBS + 80μM H_2O_2. ***P< 0.0001 comparisons between HEC_{MTP} and HEC_{MTP} + 80μM H_2O_2 at equivalent timepoints, two-way ANOVA with Tukey's multiple comparison test. Graph shows mean ± s.e.m., n = 3 per group. **(F)** Change in wet mass of HEC_{HEX}, HEC_{OCT} or HEC_{MTP} coatings over 7d exposed to either PBS or PBS + 80μM H_2O_2. *P< 0.04, ***P <0.0005, and not significant (ns) comparisons are made between HEC_{HEX} or HEC_{OCT} with HEC_{MTP} at equivalent timepoints, two-way ANOVA with Tukey's multiple comparison test. Graph shows mean ± s.e.m., n = 4 for HEC_{HEX} and HEC_{OCT} and n = 3 for all other groups. **(G)** %Change in dry mass of HEC_{HEX}, HEC_{OCT} or HEC_{MTP} coatings incubated in PBS or PBS + 80μM H_2O_2 over 7d. ***P< 0.0001, and not significant (ns) compared to HEC or as designated, one-way ANOVA with Tukey's multiple comparison test. Graph shows mean ± s.e.m. with individual data points showing n = 4 for HEC_{HEX} and HEC_{OCT} and n = 3 for all other groups. **(H)** FTIR and first derivative of FTIR of HEC, HEC_{MTP} and HEC_{SO} films in -OH region showing increase in intermolecular H-bonds. First derivative was smoothed (0th order, 200 neighbors) and inverted.

HEC_{MTP} coatings and films show oxidation-driven changes in mechanical properties

Polymer coatings or films that effectively reduce the cell-perceived mechanical stiffness of the underlying medical device may promote improved biocompatibility. As such, there has been recent interest in engineering mechanically adaptable materials which are capable of *in situ* softening once implanted *in vivo* to further improve biocompatibility outcomes (*77*). We hypothesized that the oxidation-induced increase in surface hydrophilicity and hydration observed for HEC_{MTP} coatings under physiologically relevant conditions may also confer a concurrent reduction in mechanical stiffness, making it an effective mechanically adaptable material. To test this premise, we assessed the mechanical properties of HEC_{MTP} coatings in a number of different ways and benchmarked results against HEC and a crosslinked ethoxylated polyol (CEP)-based control (**Table S5**). We first conducted lap shear testing to evaluate polymer coating adhesion and interfacial shear strength in the dry state on a glass substrate. HEC_{MTP} coatings displayed a higher ultimate interfacial shear strength (2782 kPa) at failure relative to HEC (1158 kPa) and CEP (376 kPa) coating benchmarks (**Fig. 4A-B, S18**). The observed adhesive strength of HEC_{MTP} on glass in the dry state makes it comparable to the performance of commonly used n-butyl-2-cyanoacrylate -based surgical glues under equivalent testing parameters (*78*). Both HEC_{MTP} and HEC coatings failed in lap shear tests by a combination of cohesive and adhesive failure whereas the CEP-based interface failed by a purely adhesive failure mechanism (**Fig. S18**). The strong glass substrate adhesive properties of HEC_{MTP} coatings were maintained after 7 days of incubation in PBS and we observed minimal change in coating adhesion under mild oxidizing conditions (80μM H_2O_2). However, oxidation at supraphysiological concentrations of H_2O_2 (>640μM) for just one day caused HEC_{MTP} coatings to readily delaminate due to widespread conversion of polymer thioether groups to sulfoxides, which ultimately results in bulk material changes that are not seen under physiological oxidizing conditions. Next,

we evaluated HEC_{MTP} films by tensile testing to assess how different oxidizing conditions alter bulk mechanical properties. HEC_{MTP} films in the dry state behaved as tough plastics with an elastic modulus of 455 MPa but softened significantly when equilibrated for 7 days in PBS such that the elastic modulus decreased by almost 3 orders of magnitude to 597 kPa and the hydrated material displayed behavior characteristic of a thermoplastic elastomer (**Fig. 4C-D, S19**). Hydration alone reduced the ultimate tensile strength of HEC_{MTP} by over an order of magnitude, from 30.1 MPa to 894 kPa. However, engineering strain at failure increased nearly three-fold, from 0.53 to 1.38 (**Fig. S19**). Oxidation of HEC_{MTP} films with 80μM H_2O_2 for 7 days caused no significant change in the elastic modulus, ultimate tensile strength (UTS), or strain to failure compared to the PBS incubated sample, indicating that conditions sufficient to oxidize the surface of the film provoked minimal bulk material changes. Exposing HEC_{MTP} films for 4 days to supraphysiological concentrations of H_2O_2 (800μM) that provoked detectable bulk physical changes to films as noted above resulted in a material that was softer (Elastic modulus of 233 kPa), weaker (71% reduction in UTS), and more brittle (13% decrease in strain at failure) (**Fig. 4D, S19**). To assess whether physiologically relevant oxidation conditions that do not induce bulk material changes could otherwise promote changes in the surface mechanical properties of fabricated HEC_{MTP} coatings, we performed contact-mode atomic force microscopy (AFM) to determine the micromechanical properties of the material interface after one day of hydration in PBS, then after 7 days of exposure to 80μM H_2O_2. This physiologically relevant oxidation of HEC_{MTP} coatings promoted a significant and nearly 3-fold decrease in surface elastic modulus, reducing it from 1718kPa to 674kPa (**Fig. 4E**).

These data show that HEC_{MTP} forms strongly adhered coatings on glass substrates and that exposure to physiologically relevant oxidizing conditions promotes an effective softening of the surface without imparting bulk changes to HEC_{MTP} coatings and films. Given that surface softening can readily occur under physiologically relevant oxidizing conditions, HEC_{MTP} can be considered a mechanically adaptable material that should soften when implanted *in vivo*.

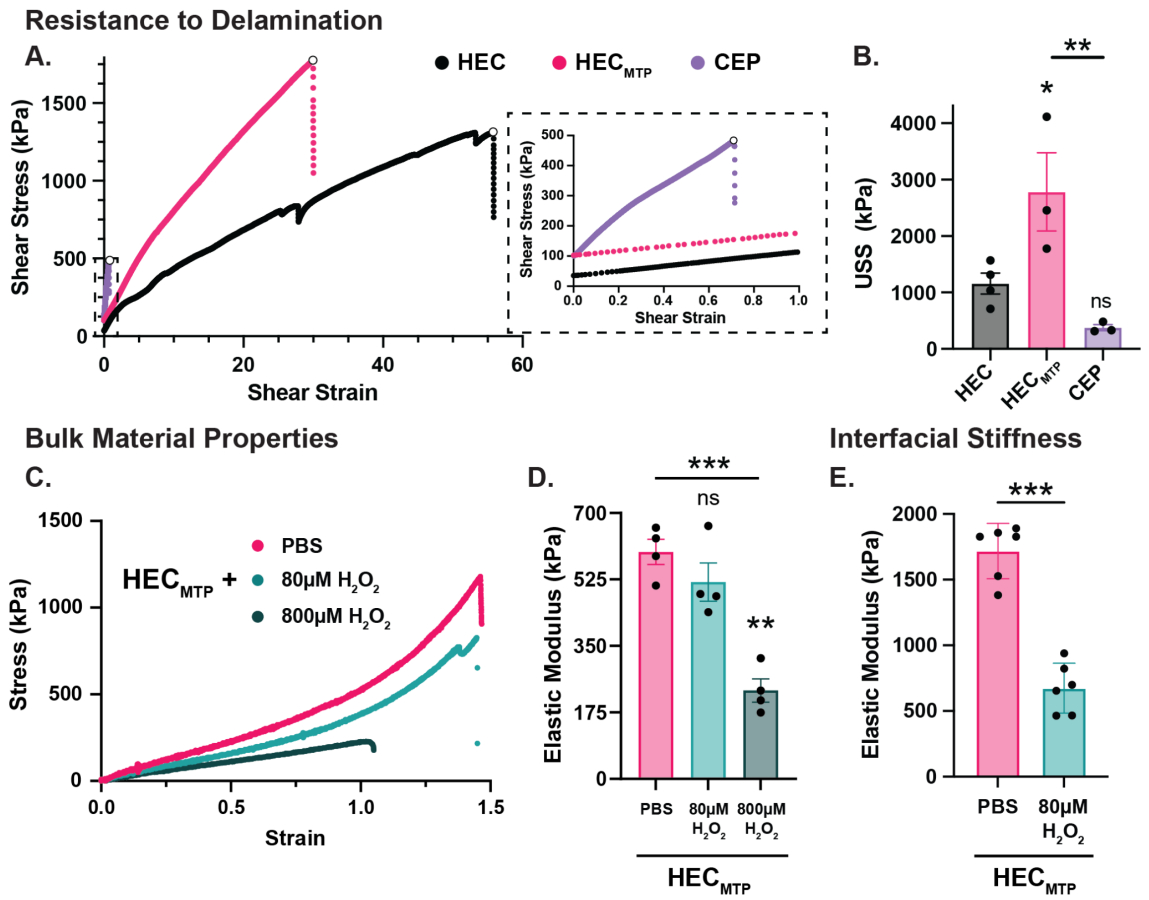

Fig. 4: HEC$_{MTP}$ coatings are resistant to delamination and demonstrate softening on oxidation. (A) Graph showing representative trace for lap shear test of HEC, HEC$_{MTP}$, and CEP coatings on glass. Inset: Detailed trace from 0.0 to 1.0 shear strain showing the CEP coating failure. **(B)** Bar graph showing the ultimate shear stress (USS) for HEC, HEC$_{MTP}$, and CEP coatings on glass. *P<0.05, **P< 0.009, and not significant (ns), one-way ANOVA with Tukey's multiple comparison test. Graph shows mean ± s.e.m. with individual data points showing n = 4 for HEC, and n = 3 per group. **(C)** Graph showing representative trace for tensile test of HEC$_{MTP}$ films incubated for 7d in PBS, 7d in PBS + 80μM H_2O_2, or 4d in PBS + 800μM H_2O_2. **(D)** Bar graph showing the elastic modulus for HEC$_{MTP}$ films, incubated for 7d in PBS, 7d in PBS + 80μM H_2O_2, or 4d in PBS + 800μM H_2O_2. **P<0.002, ***P< 0.0004, and not significant (ns), one-way ANOVA with Tukey's multiple comparison test. Graph shows mean ± s.e.m. with individual data points showing n = 4 per group. **(E)** Bar graph showing elastic modulus of HEC$_{MTP}$ coatings incubated in PBS for 1d, then measured by atomic force microscopy (AFM) before and after incubation in PBS + 80μM H_2O_2 for 7d. ***P< 0.0001, Student's t-test (paired). Graph shows mean ± s.e.m. with individual data points showing n = 6.

HEC_{MTP} coatings can be used for optical applications

Optical devices, such as probes, microprisms, optical windows, and GRIN (Gradient-Index) lenses, incorporate transparent glass windows or fibers to image and/or optogenetically control cell functions *in vivo*. However, these optical devices often experience signal instability issues or chronic noise artifacts due to deleterious FBRs stimulated by device implantation (*79*). In anticipation of a potential application for HEC_{MTP} as a surface coating on implanted optical devices to improve *in vivo* performance, we tested the optical properties of HEC_{MTP} coatings to establish their potential compatibility with such devices. Applying HEC_{MTP} coatings to transparent glass caused no observable distortion of underlying features under brightfield microscopy (**Fig. 5A**), which we validated using an established, no-reference image quality assessment (*80*) to calculate image sharpness (**Fig. 5B**). HEC_{MTP} coatings did not attenuate transmitted light within the full spectrum tested from ultraviolet (UV) (300nm) to infrared (IR) (900nm) as assessed by UV-Vis spectroscopy (**Fig. 5C**). Brightfield images and UV-Vis spectra measured through glass alone as well as HEC_{MTP} and oxidized HEC_{MTP} coatings demonstrated no detectable change in sharpness (**Fig. 5B**) or transmittance (**Fig. 5C**), whereas semi-opaque tape and black ink benchmarking controls effectively decreased both transmittance and sharpness in the visible wavelengths (400-700nm) by over 57% (**Fig. 5B-C**).

To assess HEC_{MTP} coating compatibility with fluorescence microscopy, we first stained coronal mouse brain slices (40µm thick) using a DAPI nuclear stain (**Fig. 5D**) or primary antibodies for NeuN (neuronal nuclear stain) followed by secondary antibodies conjugated with different common fluorophores that have excitation and emission wavelengths spanning the visible light spectrum (**Fig. S20**) and imaged them using a widefield fluorescence microscope. We then calculated the relative change in image sharpness when imaging through HEC_{MTP}-coated coverslips (35µm coating thickness) compared to uncoated, glass-only coverslips (**Fig. 5D-E, S20**). Qualitative (**Fig. 5D, S20**) and quantitative (**Fig. 5E**) assessments both demonstrated that the HEC_{MTP} coatings caused no appreciable change in image sharpness relative to the images taken using the uncoated glass. To confirm that this result was not simply caused by limited dynamic range of the scoring algorithm, we also applied standard Gaussian smoothing to the DAPI images, which imparts an incremental and defined blurring of the labeled nuclei (**Fig. 5D**). As expected, the application of Gaussian filters of increasing size results in significant reductions in image sharpness, contextualizing the lack of any appreciable shift in image sharpness imparted by HEC_{MTP} coatings (**Fig. 5E**).

Next, to further assess any conferred optical effects of our biomaterial in fluorescence microscopy applications, we tested the effect of HEC_{MTP} and oxidized films of different thicknesses on the apparent distortion of sub-diffraction-sized fluorescent beads, when imaged with two-photon microscopy (2PM). Imaging objects such as these beads that are smaller in size than the diffraction-limited resolution of the microscope creates a bead image of larger apparent size, with its fluorescent intensity profile parametrized by a Gaussian distribution in three dimensions. While the ideal apparent bead diameter is equivalent to the diffraction-limited resolution of the imaging system, optical scattering can lead to larger than ideal diameters, ultimately limiting resolution of the image. HEC_{MTP} films were created at thicknesses varying between 25 and 150µm, and then hydrated in PBS for 7 days, while oxidized films at the maximally wettable state were created by incubating dry HEC_{MTP} films in 10mL of 80 µM H_2O_2 in PBS for 7 days. After fluorescent beads were dried onto glass slides, the samples were covered with

mounting media and then biomaterial films, press-fit onto glass coverslips, were layered over the top. Compared to a coverglass-only control, imaging through HEC_{MTP} and oxidized films visibly altered the lateral point spread function (PSF) of the beads, as shown by one-dimensional Gaussian fits of lateral fluorescent intensity profiles taken through the center of the bead (**Fig. 5F**). Changes in apparent resolution were derived from differences in the full width at half maximum (FWHM) for each Gaussian curve, which describes the apparent diameter of the bead. The bead FWHM detected through HEC_{MTP} films showed a small but significant increase compared to the glass only controls, and this deviation was significantly correlated with film thickness (r=0.95) (**Fig. 5G**). However, there was no apparent change in conferred resolution between HEC_{MTP} and oxidized films at equivalent film thicknesses (**Fig. S20**).

These data show that HEC_{MTP} coatings and films are suitable for diverse optical applications requiring resolution down to the micron scale. While HEC_{MTP} films ultimately impacted fluorescent image resolution on the order of nanometers, the broad array of tested optical applications suggests that sufficiently thin HEC_{MTP} coatings and films are compatible with optical devices, and that this compatibility is not affected by the oxidation-driven, hydrophobic-to-hydrophilic transition.

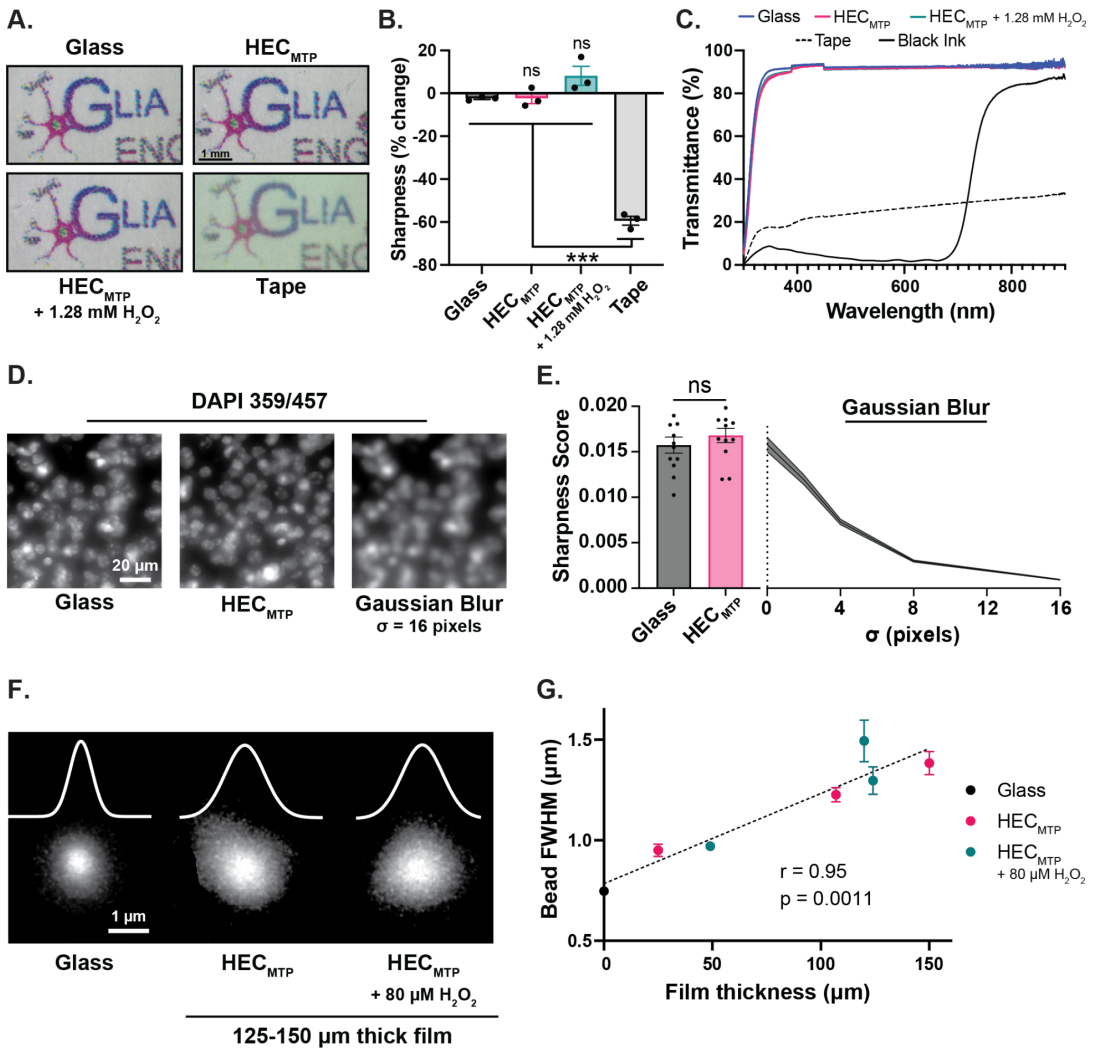

Fig. 5: HEC_{MTP} minimally scatters visible and fluorescent light, enabling optical applications. (A) Representative brightfield images of printed Glia Engineering logo covered by a glass coverslip with no coating, HEC_{MTP}, HEC_{MTP} + 1.28mM H_2O_2 for 1d, or opaque tape. **(B)** Graph showing the sharpness %change relative to ground truth (the logo without the coverslip). Not significant (ns) and ***P <0.0001 compared to glass or as designated, one-way ANOVA with Tukey's multiple comparison test. Graph shows mean ± s.e.m. with individual data points showing n = 3 for all groups. **(C)** Graph showing UV-Vis trace from 300-900nm for glass coverslips that are: uncoated, or have black ink, tape, HEC_{MTP} or HEC_{MTP} + 1.28mM H_2O_2 for 1d coatings applied. Each trace shows mean ± s.e.m., with s.e.m. represented as light shaded areas. **(D)** Widefield fluorescence images showing DAPI-stained, coronal, murine brain sections with and without a HEC_{MTP} coating on the glass coverslip, or with a Gaussian Blur filter. **(E)** Bar graph showing the sharpness scores for images of murine brain sections with uncoated or HEC_{MTP} coated glass coverslips. Not significant (ns), Student's t-test. Graph shows mean ± s.e.m. with individual data points showing n = 12 images per group. Line plot showing the sharpness scores of images of brain sections with uncoated glass coverslips with Gaussian filters of increasing size applied. Trace shows mean ± s.e.m., with s.e.m. represented as light shaded areas, and n = 12 images per group. **(F)** 2-photon fluorescent images of sub-resolution fluorescent beads, covered with a glass coverslip or a glass coverslip with a press fit film of either HEC_{MTP} or HEC_{MTP} + 80μM H_2O_2 for 7d. Overlaid traces are one-dimensional Gaussian fits characterizing the bead point spread function (PSF). **(G)** Graph showing the average apparent size of sub-resolution fluorescent beads as a function of film thickness for an uncoated glass coverslip or a glass coverslip with a press fit film of either HEC_{MTP} or HEC_{MTP} + 80μM H_2O_2 for 7d. Apparent size was measured by the full width at half maximum (FWHM) of a 1D Gaussian fit. Graph shows mean ± s.e.m. with n = 3 beads per group. Line shows linear regression of all data points and the correlation is reported as Pearson's Correlation Coefficient (r).

HEC_{MTP} films promote oxidation-responsive, controlled release of molecules

Poly(propylene sulfide)-based copolymers have been used to formulate oxidation-sensitive drug delivery systems which can selectively release drug cargo via the hydrophobic-to-hydrophilic transition stimulated by sulfoxide formation (*81*). Inspired by these studies, we next tested the capacity for HEC_{MTP} films to act as oxidation-responsive controlled release systems using fluorescently detectable model small molecules and polysaccharide-based macromolecules (**Fig. 6A-B**). To characterize small molecule release from HEC_{MTP} films, we used three coumarin derivatives that have different relative hydrophobicities including 4-methylumbelliferone (4MU) (logP = 1.78), 7-Diethylamino- 4-methylcoumarin (C1) (logP=2.90), and coumarin 6 (C6) (logP=4.79). We observed first order release profiles for both 4MU and C1 with rate constants scaling with log P values such that there was complete recovery of loaded 4MU and C1 after 3 and 8 days respectively (**Fig. 6A**). Due to its limited aqueous solubility, C6 showed limited release from HEC_{MTP} films under PBS-only incubation over 14 days. The addition of 0.1% triton-X100 surfactant into the incubation media subsequently promoted a sigmoidal pattern of release for C6, resulting in near total recovery over the subsequent 14 days (**Fig. 6A**).

To model macromolecule loading and release kinetics, FITC-dextrans with molecular weights of 10, 70, and 150kDa were incorporated into HEC_{MTP} films. These model macromolecules have matched hydrophilicities but hydrodynamic radii that are proportional to molecular weight (*82*). All model dextrans exhibited a modest initial burst release from HEC_{MTP} films when incubated in PBS which was greatest for the 10kDa FITC-dextran at 26%. By 5 days, approximately 41% of total 10kDa dextran cargo was released after which there was only minimal additional release up to 14 days. (**Fig. 6B**). Over the same 14 day period, only ~20% of the total loaded 70 and 150kDa FITC-dextrans were released from HEC_{MTP} films showing minimal but steady release after 7 days. To test for oxidation-stimulated release of the residual dextran cargo in these HEC_{MTP} films, we exposed films to 80μM H_2O_2 for 7 days followed by 320μM H_2O_2 for an additional 7 days. The 80μM H_2O_2 media promoted no significant increase in the rate of dextran release relative to the preceding 7 days in PBS only (**Fig. 6C**). However, at 320μM H_2O_2 there was a significant near 3-fold increase in the release rates for all dextrans (**Fig. 6C**).

To further dissect the oxidation-sensitive release properties of HEC_{MTP} films, we studied the initial release profiles of freshly prepared films loaded with 70kDa FITC-dextran under 80μM and 800μM H_2O_2 oxidizing conditions, which we established induces surface and bulk hydrating effects respectively. FITC-dextran released from films exposed to physiologically relevant 80μM H_2O_2 showed a near constant, zeroth order release profile following the first day burst which is consistent with molecular release being mediated by material surface hydrating effects (**Fig. 6D-E, S21)**. Under these oxidizing conditions, approximately 42% of loaded cargo had been released after 20 days, which was over double the total amount that was released from PBS-only incubated samples during the same timeframe. Incubating films in 800μM H_2O_2 resulted in an additional and significant increase in both the total amount and rate of FITC-dextran release, with over 65% of FITC-dextran recovered after just 10 days. Under these supraphysiological oxidizing conditions, the molecular release profile showed first order release kinetics, consistent with bulk-hydration of the material (**Fig. 6D-E, S21)**. Next, to test the capacity for HEC_{MTP} films to promote on-demand molecular release upon H_2O_2 exposure, we introduced intermittent 24 hour pulses of 800μM H_2O_2 to dextran-loaded films after 2, 5, and 8 days of incubation in PBS-only solutions. There was a significant spike in dextran release after each of the three intermittent exposures to H_2O_2 and release was attenuated upon removal of the oxidizing stimulus (**Fig. 6F**). Since tissue environments at chronically implanted medical devices or wounds can experience local fluctuations in ROS that can be provoked by new injuries or chronic infections, the on-demand release properties of HEC_{MTP} films may be useful for dynamically delivering drugs to regulate such responses. These data show that HEC_{MTP} films can serve as effective oxidation-sensitive drug delivery systems and are capable of loading, controllably releasing, and protecting diverse molecular cargo.

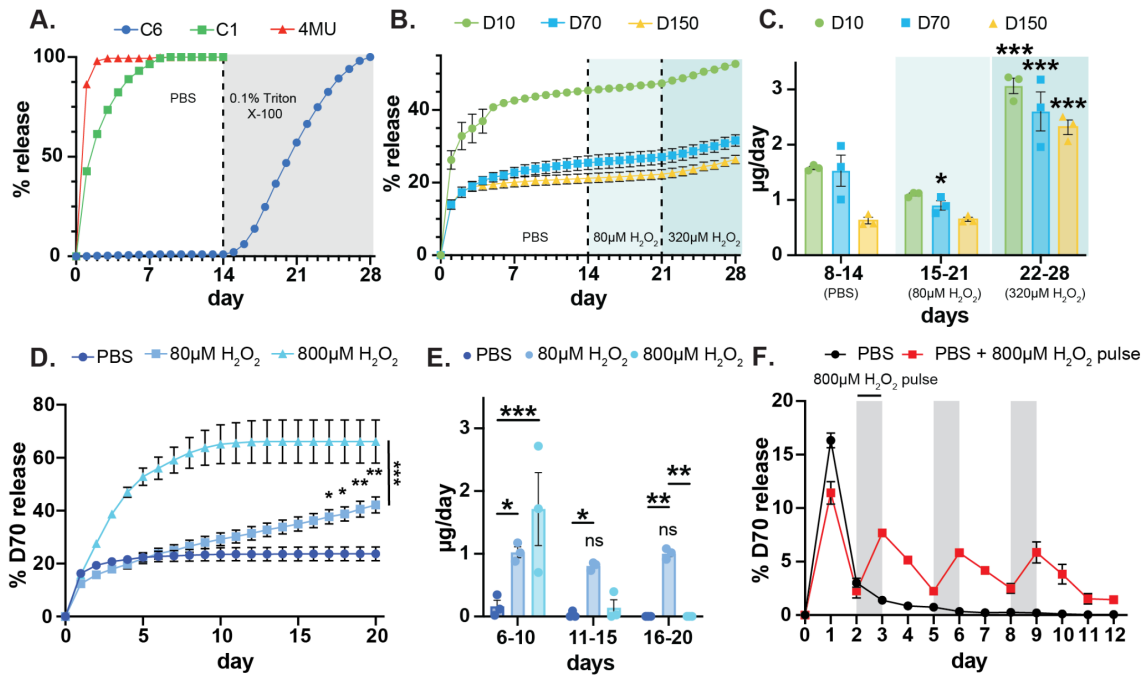

Fig. 6: HEC$_{MTP}$ coatings demonstrate controlled drug release. (A) Graph showing 28d release profile for Coumarin 6 (C6), 7-Diethylamino-4-methylcoumarin (C1), and 4-methylumbelliferone (4MU). Molecules were released into PBS (d0-d14) or PBS + 0.1% Triton X-100 (d15-d28). **(B)** Graph showing 28d release profile for FITC-dextran polymers (10kDa, 70kDa, and 150kDa). Polymers were released into PBS (d0-d14), PBS + 80μM H_2O_2 (d15-d21), or PBS + 320μM H_2O_2 (d22-d28). **(C)** Graph showing the average daily dextran for release from d8-d14, d15-d21, and d22-d28. All statistical comparisons are made with the previous duration (ie. D10 d22-d28 is compared with d15-d21) *P<0.05, ***P< 0.0007, and not significant (ns), two-way ANOVA with Tukey's multiple comparison test. Graph shows mean ± s.e.m. with individual data points showing n = 3 per group. **(D)** Graph showing 20d release profile for 70kDa FITC-Dextran (D70) from HEC$_{MTP}$ films into PBS, PBS + 80μM H_2O_2, or PBS + 800μM H_2O_2. *P<0.05, **P<0.008, ***P<0.0005 compared to PBS or as designated (between PBS + 80μM H_2O_2 and PBS + 800μM H_2O_2 from d3-d20), two-way ANOVA with Tukey's multiple comparison test. Graph shows mean ± s.e.m. with individual data points showing n = 3 per group. **(E)** Graph showing the average daily D70 release from d6-d10, d11-d15, and d16-d20. *P<0.05, **P<0.008, ***P<0.0002 compared to 6-10 80μM H_2O_2 or as designated, two-way ANOVA with Tukey's multiple comparison test. Graph shows mean ± s.e.m. with individual data points showing n = 3 per group. **(F)** Graph showing 12d daily D70 release profile into PBS with pulses of PBS + 800μM H_2O_2 at 2d intervals.

HEC_{MTP} films are nonfouling substrates that persist *in vivo* with minimal foreign body response for up to 4 weeks

To test the cytocompatibility of HEC_{MTP} coatings, we first cultured quiescent mouse astrocytes on surfaces coated with HEC, HEC_{MTP}, or HEC_{MTP} oxidized to its maximal wettability state with 320µM H_2O_2 incubation. Astrocytes are a principal cell type involved in the central nervous system foreign body response (FBR) to biomaterials *in vivo,* and therefore represent an appropriate cell type for initial *in vitro* evaluations (*82*). Astrocytes plated on either of the three experimental coatings showed no significant decrease in cell viability relative to tissue culture plastic controls (**Fig. 7A**). Next, we characterized astrocyte adhesion to coatings made from HEC_{MTP} and HEC_{MTP} pre-treated with incrementally increasing concentrations of H_2O_2 spanning physiological and supraphysiological values. While cultured astrocytes completely adhered and readily spread onto tissue culture plastic, astrocyte adhesion was reduced by more than 57% on HEC_{MTP} coatings, with cells coalescing into discrete multi-cellular aggregates that were approximately 100 µm in diameter (**Fig. 7B-C**). Oxidized HEC_{MTP} coatings exposed to at least 20µM H_2O_2 showed further attenuated astrocyte adhesion with less than 5% total cell fouling detected across all oxidized HEC_{MTP} conditions. Such minimal cell adhesion was equivalent to that noted on HEC-only coated substrates and is consistent with results observed for other sulfoxide-based materials (*60*) (**Fig. 7B-C**). The attenuated cell fouling results were likely conferred by minimal protein adsorption to HEC_{MTP}-based substrates, since HEC_{MTP} and oxidized HEC_{MTP} films showed a nearly 94% reduction in total albumin adsorption compared to a gelatin benchmarking surface by *in vitro* testing (**Fig. S22**).

Having established that HEC_{MTP} coatings are cytocompatible and minimally cell and protein fouling *in vitro*, we next assessed the stability and FBRs of HEC_{MTP} films *in vivo*. Before HEC_{MTP} films could be implanted *in vivo*, we first tested their resilience to standard sterilization methods including autoclaving and soaking in alcohol solutions. We identified minimal changes in HEC_{MTP} dry mass across all conditions (<1%), but soaking HEC_{MTP} coatings in 70% IPA overnight led to a 5-10% decrease in optical transmittance across the 300-900nm spectrum. Based on these findings, autoclaving was deemed to be the most appropriate sterilization method for HEC_{MTP} coatings and films (**Fig. S23**). To evaluate the biocompatibility and FBR to the HEC_{MTP} material, we prepared free-standing 3mm diameter HEC_{MTP} films at ~115µm thickness using an optimized fabrication method (**Fig. 2I**). HEC_{MTP} films were sterilized by autoclave and hydrated in sterile PBS for one day before use. Films of HEC_{HEX}, HEC_{OCT}, and regenerated cellulose (RC) served as benchmarking controls for this *in vivo* FBR analysis. RC films demonstrated limited swelling (144%) after one day and negligible degradation after 7 days, making the physical properties of RC suitable for comparison with HEC_{MTP} (**Fig. S24**). Despite the noted swelling and degradation limitations of the HEC_{HEX} and HEC_{OCT} materials (**Fig. S24**), we proceeded with evaluating the FBRs of all four materials (HEC_{MTP}, HEC_{HEX}, HEC_{OCT}, and RC) *in vivo* in mice.

For FBR evaluations, we implanted films subcutaneously in pro-fibrotic, C57BL/6 mice by placing hydrated films into pockets made bilaterally in the fascia tissue plane immediately below the panniculus carnosus (PC) muscle layer of the skin in regions on the back just above the hindlimbs. After 4 weeks, we perfused mice and excised skin encompassing the implant site for gross and histological analysis (**Fig 7D-E, S25**). On gross inspection we noted persistence of all implanted HEC_{MTP} films at 4 weeks with minimal change in size, morphology, or transparency. For some, but not all, HEC_{MTP}

treated mice, films readily separated from the subcutaneous implant site on dissection due to sparse peri-implant tissue around the film and we were able retrieve these samples as intact films (**Fig. 7F, S25**). Neither HEC_{HEX} or HEC_{OCT} films could be identified on gross inspection, however obvious localized regions of differentially-colored scar tissue remained at the implant sites for mice receiving these materials. Histology of explanted films by hematoxylin and eosin (H&E) and Masson's Trichrome (MT) staining revealed thin and loose peri-implant tissue around HEC_{MTP} films with minimal numbers of persisting immune cells at the film surface and no cell infiltration into the bulk of the material (**Fig 7D-E, S26**). By contrast, both HEC_{HEX} and HEC_{OCT} films showed significant immune cell infiltrates and collagen-rich fibrosis that penetrated throughout pockets of residual polymer material. HEC_{HEX} promoted a more severe immune response compared to all other tested materials with immune cells having larger nuclei as well as cytoplasms that were more basophilic (**Fig 7D-E, S26**). There was a greater extent of immune cell infiltration and fibrosis with organized collagen fibers permeating throughout the implant site in animals receiving HEC_{HEX} compared to all other groups. The immune response to HEC_{OCT} showed notably paler immune cells with more condensed nuclei and large, clear cytoplasmic vacuoles consistent with foamy macrophages, which was unique to this material. Meanwhile, examination of peri-implant tissue at RC films revealed a fibrotic capsule that had a similar abundance of recruited immune cells as HEC_{MTP} both within the fibrotic tissue layers above and below the RC film as well as deposited along the material-tissue interface (**Fig 7D-E, S26, S27A-B**). Quantification of peri-implant fibrotic capsule thickness inclusive of the superficial and deep layers measured from the end of the PC muscle layer verified that HEC_{MTP} films were not significantly different from RC, a widely used, biocompatible biomaterial, and promoted a significantly less severe FBR compared to both HEC_{HEX} and HEC_{OCT} films (**Fig 7G**). Further analysis of the deep fibrotic capsule layer and dense collagen layer around HEC_{MTP} and RC films revealed no significant differences between the two biomaterials (**Fig 7H, S27**). HEC_{MTP} films retrieved from mice after 4 weeks had a small, but detectable, increase in hydrated mass compared to pre-implant films and chemical characterization of retrieved films by FTIR showed changes in the hydroxyl and thiocarbamoyl stretch regions consistent with oxidation-induced sulfoxide conversion of some of the thioether groups along the HEC_{MTP} polymer chain (**Fig 7I**).

These data show that HEC_{MTP} films are cytocompatible and form non-fouling interfaces upon exposure to physiologically relevant oxidizing conditions. HEC_{MTP} is non-resorbable and persists for up to 4 weeks *in vivo* with minimal induced FBR or physical property changes, which was uniquely conferred by its functionalization with MTP groups. Sulfoxide conversion of the pendant thioether groups on the polymer chains in explanted films demonstrated that HEC_{MTP} can undergo the hydrophobic-to-hydrophilic transition *in vivo* under physiological conditions and serves as proof-of-principle evidence that justifies the future exploration of HEC_{MTP} for applications as an oxidation-responsive biomaterial.

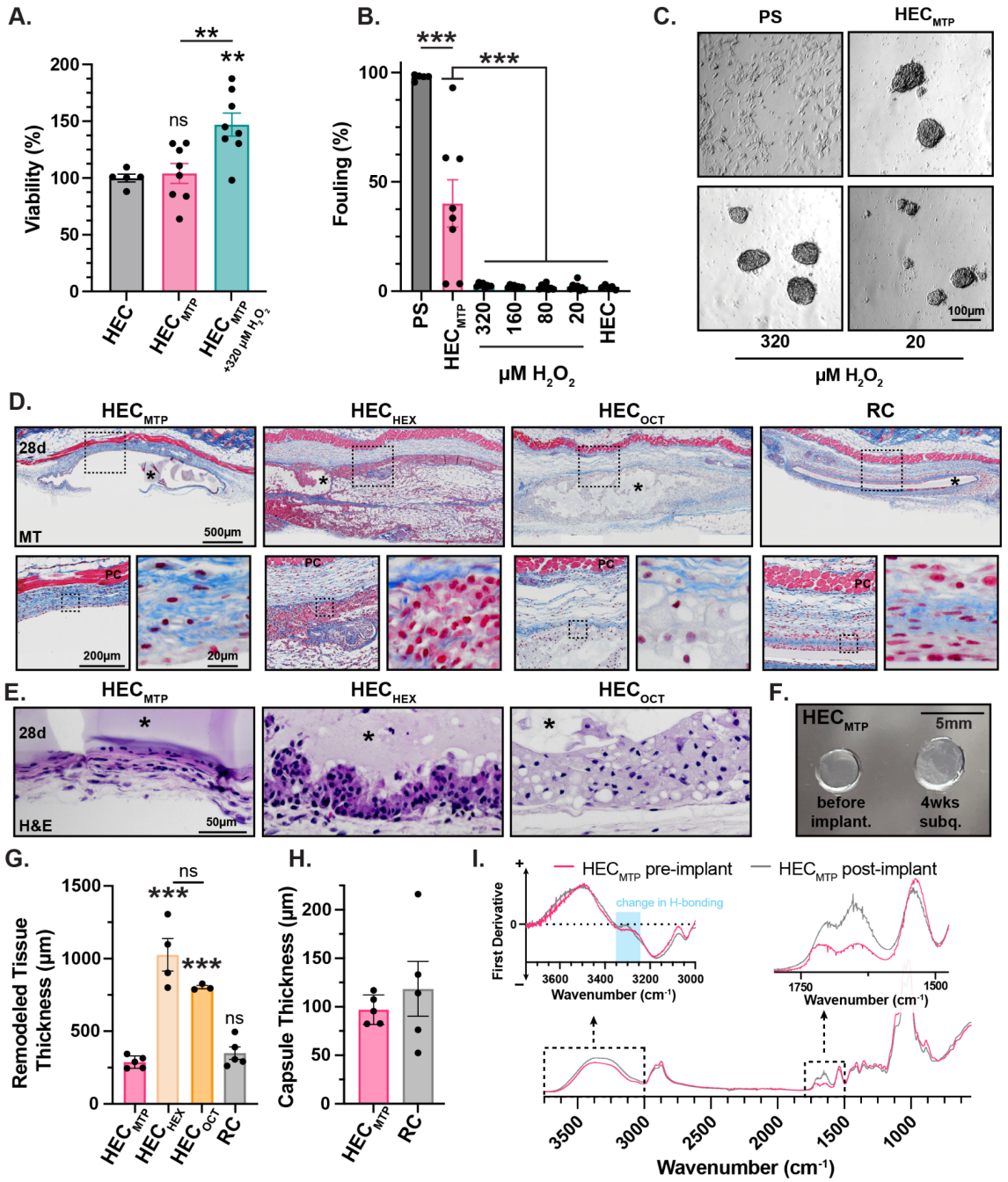

Fig. 7: HEC_{MTP} materials are non-fouling *in vitro* and *in vivo*. (A) Cytotoxicity assay using Calcein AM demonstrates that coatings of HEC, HEC_{MTP}, and HEC_{MTP} treated with 320µM H_2O_2 are cytocompatible. Not significant (ns) and **P <0.008 compared to HEC, one-way ANOVA with Tukey's multiple comparison test. **(B)** Oxidation of HEC_{MTP} with all concentrations of H_2O_2 leads to a significant decrease in astrocyte fouling relative to an untreated polystyrene (PS) surface. ***P <0.0001, one-way ANOVA with Tukey's multiple comparison test. **(C)** Phase contrast images showing morphology of cells seeded on an untreated polystyrene (PS) surface, HEC_{MTP}, and HEC_{MTP} treated with either 320 or 20µM H_2O_2. **(D)** Survey and detail images of histology sections stained with Masson's Trichrome (MT) showing implant site and foreign body response (FBR) to subcutaneously implanted HEC_{MTP}, HEC_{HEX}, HEC_{OCT}, and regenerated cellulose (RC) films after 28d. Materials are marked with * and the

panniculus carnosus with PC. **(E)** Detail images of histology sections stained with hematoxylin and eosin (H&E) showing FBR to subcutaneously implanted HEC_{MTP}, HEC_{HEX}, and HEC_{OCT} films after 28d. Materials are marked with *. **(F)** Brightfield images of hydrated HEC_{MTP} films before and after 4wk subcutaneous (subq) implantation. **(G)** Quantification of remodeled tissue thickness for HEC_{MTP}, HEC_{HEX}, HEC_{OCT}, and RC films. Not significant (ns) and ***$P \leq 0.0003$, one-way ANOVA with Tukey's multiple comparison test. Graph shows mean ± s.e.m. with individual data points showing n = 3 for HEC_{OCT}, n = 4 for HEC_{HEX}, and n = 5 for HEC_{MTP} and RC. **(H)** Quantification of deep capsule thickness for HEC_{MTP} and RC films. Graph shows mean ± s.e.m. with individual data points showing n = 5 per group. **(I)** FTIR of HEC_{MTP} films pre- and post-implantation. Dashed boxes highlight regions of interest from 1500-1750 cm^{-1} and 3000-3750 cm^{-1}. First derivative was smoothed (0th order, 100 neighbors) and inverted.

Discussion

Performance longevity of chronically implanted medical devices remains a significant challenge. Hydrophilic polymer coatings or films are a potential way to prevent premature device failure by improving overall biocompatibility. However, issues such as swelling, delamination, and manufacturing scale-up have hampered the effective incorporation of existing coating and film technologies into medical devices (*32–41*). Here, we addressed these issues by functionalizing a readily sourced and inexpensive cellulose derivative, HEC, with thioether groups via a one-pot, isothiocyanate-based reaction to generate a new, oxidation-responsive biomaterial, HEC_{MTP}. HEC_{MTP} can be fabricated into stable, minimally swelling coatings or films that undergo oxidation-driven hydrophobic-to-hydrophilic transitions under physiological conditions to generate non-fouling and mechanically adaptable substrates. Our findings demonstrate proof-of-principle that HEC_{MTP} is a biocompatible and non-resorbable biomaterial *in vivo* and has implications for: 1) extending the functionality of cellulose-based material coatings and films; 2) incorporating HEC_{MTP} coatings/films onto optical devices, and 3) using HEC_{MTP} for acute inflammation resolution to improve medical device biocompatibility.

Cellulose is an abundant, inexpensive, and sustainable polymer feedstock that has provided significant societal value over the past century (*42*, *53*). Cellulose-based materials continue to have broad impact across many industrial applications because of their versatile physical and chemical properties which can be tuned by modifications to polymer structure including the degree and type of chemical substitutions on the repeating anhydroglucose unit (*55*). Here, we add to the growing list of permitted chemical modifications to cellulose materials by developing HEC_{MTP}, a new thioether functionalized cellulose. HEC_{MTP} represents an important advance in cellulose-based materials as it can be directed to behave like either a cellulose ester or a hydrophilic cellulose derivative under different conditions, affording unique properties and processing capabilities. Cellulose esters are the predominant class of cellulose materials produced commercially in part because they can be dissolved and easily processed in organic solvents (*53*, *54*). Here, we show that HEC_{MTP} can be readily dissolved in DMSO and blends of common green solvents enabling a similar level of processability that is critical to fabricating commercially viable coatings and films. However, unlike cellulose esters which are moderately hydrophobic, HEC_{MTP} can be facilely transformed into a hydrophilic polymer by a simple, oxidation-driven conversion of pendant thioether groups to

sulfoxides. While coatings made from other hydrophilic cellulose derivatives suffer from swelling and delamination issues (*53*), the controlled hydrophobic-to-hydrophilic transition of HEC_{MTP} that occurs at the surface of the material under physiologically relevant oxidizing conditions enables the generation of a highly wettable surface without causing bulk material changes that compromise coating integrity or its adhesion to the underlying substrate. Further work will be required to optimize HEC_{MTP} solution parameters, such as polymer concentration and solvent composition, to address the protracted time required for film formation, which is a current limitation of this system, due to the low volatility of the DMSO-only solvent system. In addition to increased manufacturing speed, HEC_{MTP} formulation innovations would allow us to incorporate other coating techniques, such as layer-by-layer assembly or spin coating, to generate thinner HEC_{MTP} coatings with a more uniform surface topography than what was achieved here. Given the modular nature of the thioether functionalization method, important next steps will be to extend our approach to other cellulose derivatives, or to different molecular weight HEC, to tune chemical functionality and/or solution viscosity in order to derive coatings and films with adjustable physical and mechanical properties. Since thioether groups are susceptible to modification by alkylation reactions, the HEC_{MTP} template could also be used to generate other functional materials in future work. For example, reacting HEC_{MTP} substrates with alkyl halides would likely be an effective way to convert thioethers to sulfonium groups and generate potent antimicrobial surfaces (*59*). Also, modification of HEC_{MTP} with haloacetic acids could be used to create new zwitterionic substrates that would likely lead to further improvements in the cell and protein non-fouling properties (*13*, *59*).

Since HEC_{MTP} coatings minimally alter the optical properties of underlying glass substrates, there are exciting possibilities for their incorporation with chronically implanted optical devices such as transparent glass fibers (*83*), miniature integrated microscopes (*84*), or microprisms (*85*). Such optical devices are becoming increasingly popular tools in preclinical research, and also have emerging clinical therapy applications (*86*). However, without effective coatings to regulate implantation-induced FBRs, these optical devices will continue to be plagued by premature device failure, signal drift over time, and unresolved noise artifacts (*79*). HEC_{MTP} coatings may afford a new way to regulate FBRs at optical devices without compromising optical integrity parameters due to coating swelling or delamination-induced artifacts. However, to realize the potential of HEC_{MTP} for optical devices, more work will be needed to optimize the fabrication of uniform coatings of HEC_{MTP} onto complex device geometries. Furthermore, *in vivo* studies will be required to determine whether *in situ* oxidized HEC_{MTP} surfaces are sufficiently nonfouling to maintain the pristine optical interfaces needed for high imaging fidelity. Incorporation of selective surface oxidation of HEC_{MTP} coatings by either H_2O_2 solution incubation or plasma treatment prior to implantation could be integrated into the manufacture of these coating systems if *in situ* oxidation proves to be insufficient (*87*).

HEC_{MTP} coatings and films, in addition to modulating surface wettability and cell perceived mechanical properties of implanted medical devices, may also enable new strategies to directly regulate inflammation induced by devices. Neutrophils recruited locally to the surface of implanted medical devices during acute inflammation produce ROS and other mediators as part of antimicrobial defense mechanisms (*88*). Neutrophils are sensitive to the surface properties of medical devices and excessive or prolonged neutrophil accumulation can exacerbate device-adjacent tissue damage, cause biomaterial degradation, or prevent acute inflammation resolution necessary for progression of wound

healing processes (*89*). As such, there is growing interest in developing approaches to better control neutrophil functions at implanted medical devices (*90*). The ROS scavenging and ROS-dependent changes in surface properties of HEC_{MTP} coatings and films demonstrated here could make them an effective tool to regulate the oxidative functions of the neutrophil response, mitigate ROS-associated tissue damage, and accelerate acute inflammation resolution (*91*). Furthermore, given the oxidation-responsive, controlled release properties of HEC_{MTP} films also demonstrated here, there is an opportunity to leverage this mechanism for ROS-induced, on-demand delivery of immunoregulatory drugs to better control acute inflammation resolution locally at the sites with the highest neutrophil or ROS burden. To practically realize these strategies, further development efforts will be required to improve upon the ROS-sensitivity of the current system by carefully selecting the cellulose template and degree of thioether functionalization to better tune the physical changes to the polymer induced by the oxidation-driven, hydrophobic-to-hydrophilic transition.

In conclusion, this work describes the derivation and characterization of a new, thioether-functionalized, oxidation-responsive cellulose material. The results from this study lay the foundations for using this material to regulate the FBR to implanted medical devices, including implanted optical systems, and as an oxidation-responsive drug depot.

Materials and Methods

Materials

All solvents used in this work are certified ACS grade or higher.

From Sigma Aldrich, we purchased: 2-Hydroxyethyl cellulose (HEC) (average MW: 380kDa) (308633), 3- (methylthio)propyl isothiocyanate (MTPI) (W331201), 4-Methylumbelliferone (M1381-25G), Coumarin 6 (442631-1G), 10kDa Fluorescein isothiocyanate-dextran (FD10S-100MG), 70kDa Fluorescein isothiocyanate-dextran (FD70S-100MG), 150kDa Fluorescein isothiocyanate-dextran (46946-100MG-F), gelatin from porcine skin (G1890-100G), albumin-fluorescein isothiocyanate conjugate (A9771-250MG).

From Tokyo Chemical Industry Co (TCI), we purchased: 7-Diethylamino-4-methylcoumarin (M0631), N, N-Diisopropylethylamine (DIEA) (D1599).

From ThermoFisher, we purchased: deuterated trifluoroacetic acid (dTFA) (Cat # 325310250), Methyl sulfoxide-d6 (Cat # 364650500), hydrogen peroxide, 30% (Cat # H325-500), B27 (no Vitamin A) (50X) (Cat # 12587010), Octyl isocyanate (Cat # AC41460100), 1-Hexyl isothiocyanate (Cat # AAA1222314).

From Peprotech, we purchased: Epidermal Growth Factor (EGF) (Cat# AF-100-15-100UG), Fibroblast Growth Factor (FGF) (Cat# 100-18B-100UG).
From Gibco, we purchased: Advanced Dulbecco's Modified Eagle Medium/ Nutrient Mixture F-12 (DMEM/F12) (Ref# 12634-010), PBS pH 7.4 (1x) (Ref# 10010-023).

From Abcam, we purchased: rabbit anti-NeuN (1:1000, Abcam, ab177487).

From Jackson ImmunoResearch Laboratories, we purchased: AffiniPure™ Donkey Anti-Rabbit IgG secondary antibodies conjugated to Alexa Fluor 488 (AB_2313584), Alexa Fluor 555 (AB_3095471), Alexa Fluor 647 (AB_2492288), or Alexa Fluor 790 (AB_2340628).

From Invitrogen, we purchased: ProLong Gold anti-fade reagent (Cat# P36934).
We also purchased: Sylgard 184 (Cat# 24236-10) from Electron Microscopy Sciences, Mettler 40µL Aluminum Crucible (DSC22001) and lid (DSC22002) from DSC Consumables Inc., Calcein AM from Corning (Cat# 354217), 4',6'-diamidino-2-phenylindole dihydrochloride (DAPI) from Molecular Probe (D1306), SensoLyte® ADHP Hydrogen Peroxide Assay Kit (AS-71112) from AnaSpec, untreated microscope slides were purchased from Opto-Edu (E35.3501).

Synthesis of HEC_{MTP}, HEC_{SO}, HEC_{HEX}, and HEC_{OCT}

Prior to synthesis, 2-Hydroxyethyl cellulose (HEC) (average MW: 380kDa) was lyophilized, and dimethyl sulfoxide (DMSO), as well as N, n-diisopropylethylamine (DIEA), were dried over 4A molecular sieves for at least 24hrs. HEC was reacted with MTPI to form HEC_{MTP} via a DIEA-catalyzed nucleophilic addition (**Table S1**). Briefly, HEC and MTPI were solubilized in DMSO and purged with nitrogen for 20min before the addition of DIEA. The reaction was heated at 80°C and stirred at 300RPM for 72hrs. The reaction was purified by precipitation in ethyl acetate. The solid was then collected, redissolved in DMSO, and precipitated again in ethyl acetate. The HEC_{MTP} precipitate was

then dialyzed in deionized (DI) water for 72hrs with three water changes. HEC_{SO} materials were synthesized by oxidizing HEC_{MTP} in a 1% hydrogen peroxide (H_2O_2) solution for 24 hours. Following the reaction, the polymer was dialyzed in DI water and lyophilized as previously described. HEC_{HEX} (**Table S3**) was prepared in an identical manner to HEC_{MTP}, with the reactive molecule (MTPI) being substituted for hexyl isothiocyanate. HEC_{OCT} (**Table S4**) was prepared by first solubilizing lyophilized HEC in DMSO at 10mg/mL. Octyl isocyanate was added at the proper stoichiometry, and the reaction was started via the addition of DIEA (**Table S4**). HEC_{OCT} reaction proceeded at 25°C while stirring at 300RPM for 24hrs before being purified as previously described.

Nuclear Magnetic Resonance (NMR) Spectroscopy

^{1}H NMR was performed on an Agilent 500 MHz VNMRS spectrometer at concentrations of ~10mg/mL and a total volume of 750 µL in DMSO-d6 or dTFA as specified. The spectra were recorded at 117.42kG (1H 500MHz, 13C 125MHz) at ambient temperature. Hydrogen chemical shifts are expressed in parts per million (ppm) relative to the residual proton solvent resonance: DMSO-d6 δ2.50 or δ3.33, or dTFA δ11.50. Following the initial NMR of HEC in dTFA, all subsequent HEC-derivative NMRs were referenced to the HEC-associated peak at δ4.60.

Fourier Transform Infrared Spectroscopy (FTIR)

FTIR was performed on lyophilized polymer samples using a Nicolet 4700 FTIR-ATR between the wavenumber region 4000-400 cm^{-1} (64 scans, 0.241 cm^{-1} resolution). All FTIR spectra were baseline corrected and normalized by the total area under the curve (AUC) unless otherwise specified.

Biomaterial Film Fabrication

HEC-derived films were prepared by solubilizing dried material stocks at 3wt% in DMSO and drop-casting HEC_{MTP}, HEC_{HEX}, or HEC_{OCT} solutions in a silicone mold (150µL of solution in a 10mm diameter, silicone, circular mold). Each layer was dried in a vacuum oven at 35°C and 270 mbar for 24hrs before adding an additional layer. By applying 1 to 3 layers, films could be formed with thickness ranging from 7-70µm.

X-ray Photoelectron Spectroscopy (XPS)

HEC films were prepared by solubilizing HEC stocks, which had been previously dialyzed and lyophilized, at 6wt%. HEC solution was then pipetted into a silicone mold and dried in a vacuum oven. HEC_{MTP} films were prepared as previously described and treated with PBS or 80µM H_2O_2 in PBS for 7d or 800µM H_2O_2 in PBS for 1d and then dialyzed against water. Films were then attached to the sample platen and spectra were taken on a PHI Genesis XPS system with an Al K-alpha source after degassing overnight. Binding energy shifts were referenced to the C 1s peak at 284.8 eV.

Goniometry

Samples were prepared for goniometry by drop-casting a 3wt% polymer solution HEC or HEC_{MTP} in DMSO onto cleaned glass slides. Samples were dried in a vacuum oven for 72hrs at 35°C on house vacuum (~270 mbar). Samples were then dipped in phosphate buffered saline (PBS) for 20 seconds, blown dry, and tested (**Figure 1H**). For reactive oxygen species (ROS) exposure assay (**Figure 3D**), slides were prepared as previously described. After drying, the coated substrate was exposed to H_2O_2 at the specified concentration for 24hrs, at 37°C. Slides were then transferred to a DI water bath to quench the oxidation reaction, blown dry, and tested immediately. Goniometry was performed on

a Kruss DSA100 Contact Angle Goniometer by dropping 11µL of DI water onto glass substrates coated with polymer solution. OCA20 Software was used to measure the contact angle relative to the substrate over the course of 2 minutes immediately after dropping. Reported values are the average contact angle over this time.

Thermal Gravimetric Analysis (TGA)/Differential Scanning Calorimetry (DSC)
TGA/DSC was performed on a Mettler Toledo TGA/DSC. Polymer samples were loaded in a 40µL aluminum crucible, perforated, and tested under nitrogen (50mL/min) over a range of temperature from 30˚C to 400˚C at a rate of 10˚C/min.

Rheological Testing
Rheological testing was conducted on a TA Instruments DHR-2 Rheometer. ~200µL of polymer solution was tested during each collection. Viscosity was measured as a function of shear rate on a logarithmic scale with a sampling of five points per decade with shear rates ranging from 0.1-1000s^{-1}. Zero-shear viscosity values are represented as the viscosity values at a shear rate of 0.1s^{-1}. Temperature sweeps were performed at a shear rate of 1s^{-1} from 25-80°C. All testing was done using a 20mm 2° cone, except for the 1wt% polymer solution, which was done on a 40mm 1° cone.

Dipping Mold Fabrication and Dip-Coating Protocol
Polydimethylsiloxane (PDMS) molds were fabricated by mixing a silicone elastomer base and curing agent in a 10:1 ratio in the mold casing. The base was vacuumed for 1hr both before and after adding the curing agent. After vacuuming, a glass insert covered with aluminum foil was placed in the PDMS and placed into an oven at 30˚C for 72hrs to cure. The glass insert was removed after drying and the molds were cleaned using DMSO and acetone.

Untreated glass slides were used as a substrate for all coatings. Glass slides were bathed overnight in 1N hydrochloric acid (HCl) to ensure a clean surface. Prior to coating, slides were dipped in HCl, followed by water, then acetone, and blown dry. The pre-made PDMS molds were filled with the appropriate polymer precursor solution. An Instron 5944 Micro-tester tensile testing machine was used to control the speed at which the glass slide was dipped and thereby the shear rate at the interface of the slide. After performing initial rheological testing, it was determined that slides should be dipped at 1 mm/sec (the fastest rate that still approximately maintains zero-shear viscosity or a shear rate of 1 sec^{-1}). After dipping, glass slides were dried in a vacuum oven for 72hrs at 35°C on house vacuum (~270 mbar).

Coating Thickness and Roughness Measurements
Coating thickness was measured using a Neoteck Digital Thickness Gauge Meter with LCD Display (Range: 0.001-12.7mm/0.00005-0.5”). A Dektak Profilometer was used to measure HEC_{MTP} coating profiles. A tip radius of 5µm with 1mg of applied force was used to scan a 30000µm length over 60 seconds with a resolution of 1.667µm per sampled point and a measurement range of 65.5µm. All roughness data was processed by selecting 1000µm of the HEC_{MTP} coating profile, fitting a linear trendline, and baseline correcting the profile data using this trendline. HEC_{MTP} coating profile data was then centered on 0nm by subtracting the mean of the data from each data point. Average roughness was calculated by taking the average of the absolute value of this processed profile data.

H_2O_2 Scavenging Experiments
All H_2O_2 scavenging experiments were performed by plating 50µL of the HEC material (HEC, HEC_{MTP}, HEC_{HEX}, HEC_{OCT}) solubilized at 1wt% in DMSO in a 96-well plate and drying in a vacuum oven for 7d at 35°C on house vacuum (~270 mbar). 100µL of H_2O_2, freshly diluted from a 30% (9.8M) stock, was plated on top of the HEC_{MTP} coatings, at the appropriate concentration and read after either 24hrs or as noted using the SensoLyte® ADHP Hydrogen Peroxide Assay Kit (AnaSpec, AS-71112).

Temporal Changes in Contact Angle, Wet Mass, and Dry Mass
Measurements for contact angle, wet mass, and dry mass were performed on HEC_{MTP}, drop-cast on glass slides as previously described. The glass slides were pre-weighed to allow for accurate determination of coating mass. After drying, slides were either placed in 25mL of PBS or 80µM H_2O_2 in PBS, as designated, and incubated at 37°C. To measure wet mass, slides were removed at 1, 3, and 7d and the surface moisture was removed using compressed air, slides were then weighed on a microbalance. Contact angle was measured as previously described. Dry mass was measured by incubating coated slides for 7d, and then removing the coated slide, drying with compressed air, and lyophilizing the coated slide before weighing on a microbalance.

Lap Shear Test
Samples were prepared by drop-casting 100 µL of HEC or HEC_{MTP} onto cleaned glass slides and drying in a vacuum oven at 35°C and 270 mbar for 72 hrs. Crosslinked ethoxylated polyol (CEP) controls were prepared by first flashing poly(ethylene glycol) diacrylate (PEGDA 700) and ethoxylated trimethylolpropane tri (3-mercaptopropionate) (ETTMP 1300) over basic alumina. Next, flashed PEGDA 700 and ETTMP 1300 were mixed with 10µL of 2,2-Dimethoxy-2-phenylacetophenone (DMPA) solubilized at 20mg/mL in dimethyl sulfoxide (DMSO) (**Table S5**). This precursor solution was then drop-cast onto the glass substrate and cured under UV light (365 nm) for 1 hour. A second glass slide was then superglued (Krazy Glue, All Purpose Super Glue) to the applied sample (**Figure S18**), and the free ends of each slide were coated in epoxy (Gorilla, Clear Epoxy) and allowed to cure for 24 hours. This was employed to prevent slipping at the interface between the glass and the Instron grips, which was initially observed at high applied forces. Samples were positioned vertically with 2kN Instron 2710-114 screw side-action grip attachments. Standard tensile testing was performed at a rate of 5% of slide overlap length per minute until failure. Ultimate shear stress (USS) was defined as the maximum stress before failure.

Bulk Mechanical Testing
HEC_{MTP} films were fabricated as previously described to create films of 75-150 µm thickness. To constrain mechanical failure to the material midsection, films were then punched into a dogbone shape with gauge length 10mm and gauge width 1.5mm using a Print-A-Punch™ device (Northwest Tissue Mechanics Laboratory, Boise State University, Boise, Idaho) (*92*)**.** In addition to dry films, HEC_{MTP} films were then hydrated in PBS for 7 days or incubated in 10 mL of 80 µM H_2O_2 in PBS for 7 days. Regenerated cellulose (RC) films were punched from 1kDa RC dialysis bags (Spectrum, P/N: 132104) and hydrated in PBS for 7 days. Using an Instron 5944 Micro-tester tensile testing machine, uniaxial tensile testing was performed on all films at a rate of 1% nominal strain/sec until failure.

Atomic Force Microscopy (AFM)
Elastic modulus measurements were performed using an Asylum MFP-3D-BIOTM atomic force microscope with silicon nitride tips (Nano World, PNP-TR-Au, Force Constant: 0.32 N/m or 0.08 N/m). HEC_{MTP} was drop-cast on glass slides as previously described, with the addition of a second layer of HEC_{MTP} 24 hours after the first. Measurements were taken first after 24 hours of sample hydration in PBS, then subsequently after 7 day incubation of the same samples in 80µM H_2O_2 in PBS at 37°C. Measurements were performed in submerged contact mode, with both the sample and AFM tip completely submerged in PBS. For each sample slide, 3 replicate force-displacement curves were acquired at different locations on the sample surface. Force-displacement curves were fitted with a Hertzian viscoelastic model to determine the elastic modulus, which was reported for each sample as the mean of the replicate measurements.

UV-Vis Spectroscopy
Glass coverslips (10.5mm x 50mm x 150µm, Chemglass (CLS-1762-1050)) were coated with tape (Scotch, Matte Finish MagicTM Tape), black marker, or HEC_{MTP} solution and dried. Coverslips coated with HEC_{MTP} were additionally treated with 1280µM H_2O_2, dipped in 70% isopropyl alcohol (30% water), or autoclaved. Measurements were taken using a Hitachi U-3010 UV–vis Spectrophotometer. Spectra spanned 300–900 nm and were taken at a scan speed of 60 nm min^{-1}.

Brightfield Imaging and Image Sharpness
The 'Glia Engineering' logo was printed using a RICOH IM C3500 Color Laser Multifunction Printer onto standard printer paper. Brightfield images were taken using an Axiocam 208 color mounted microscope camera on a Stemi 305 stereo microscope (ZEISS). Image sharpness was calculated using a custom MATLAB script, which first thresholded images in the frequency domain, and then applied an adapted, no-reference scoring algorithm for quantifying image sharpness (*80*).

Widefield Fluorescence Imaging and Image Sharpness
Coronal sections of healthy murine brain were prepared and stained as previously described (*93*) either using 4',6'-diamidino-2-phenylindole dihydrochloride (DAPI; 2 ng mL^{-1}; Molecular Probes) to stain cell nuclei or primary antibodies for rabbit anti-NeuN (1:1000). Secondary antibodies were conjugated to: Alexa Fluor 488, Alexa Fluor 555, Alexa Fluor 647, or Alexa Fluor 790. All secondary antibodies were purchased from Jackson ImmunoResearch Laboratories and were affinity-purified whole IgG(H + L) antibodies with donkey host and target species dictated by the specific primary antibody used. Secondary antibodies were diluted 1:500 prior to incubation. HEC_{MTP} films were fabricated as previously described and press fit to coverslips. Coverslips were then placed over coronal sections and imaged on an Olympus IX83 epifluorescent microscope using standardized exposure times. Rectangular regions of interest (ROIs) from fluorescent images of sections with and without a HEC_{MTP} coating were generated and cropped into separate images. Image sharpness was calculated as previously described (*80*). For each fluorescent channel, conferred changes in sharpness scores were reported as the differences between the sharpness scores of a HEC_{MTP}-coated ROI and the average sharpness score of all uncoated ROIs. Additionally, changes in sharpness score were calculated for uncoated DAPI ROIs before and after Gaussian blurring filters of increasing size were applied.

Two-Photon Fluorescence Microscopy
Yellow-green fluorescent beads of 0.2 µm diameter (Polysciences, Cat# 17151) were dried onto glass slides. HEC_{MTP} films were created as previously described, with either 1 or 3 layers applied during fabrication. HEC_{MTP} films were then hydrated in PBS for 7 days or incubated in 10 mL of 80 µM H_2O_2 in PBS for 7 days. Control samples were created by covering bead samples with mounting media and a glass coverslip. HEC_{MTP} and HEC_{MTP} + 80 µM H_2O_2 samples were created by covering bead samples with a biomaterial film press-fit to a glass coverslip.

Fluorescent bead samples were excited at 950 nm and imaged on a Bruker Ultima Investigator two-photon microscope with a tunable Ti:Sapphire laser (Insight X3, Spectra Physics) and a 16x water-immersion objective (Nikon). Z-stacks were created by raster scanning across a field of view (FOV) of 25 µm x 25 µm, with a pixel size of 24.4 nm. Acquired image stacks were processed using FIJI. From the ~10 beads visible in each FOV, 3 were selected for analysis. For each bead, the axial centroid was determined from the axial intensity profile, and the corresponding image in the Z-stack was analyzed. A 3.5 µm line was manually drawn through the center of the bead, and the fluorescent intensity profile was fitted with a one-dimensional Gaussian. The full width at half maximum (FWHM) of the Gaussian fit was calculated and reported as the apparent bead diameter.

Release Assay
To measure release from HEC_{MTP} films and coatings, either small fluorescent molecules (7-Diethylamino-4-methylcoumarin (C1), coumarin 6 (C6), and 4-methylumbelliferone (4MU)) or larger FITC-dextran polymers (10kDa, 70kDa, and 150kDa) were first solubilized in DMSO at 1mg/mL and 10mg/mL, respectively. HEC_{MTP} was solubilized at 3wt% in DMSO and molecule solutions were added to achieve loading ratios of 1µg/mg and 100µg/mg for small molecules and dextrans respectively. Loaded HEC_{MTP} was either drop-cast in a glass scintillation vial to form approximately 4mg HEC_{MTP} coatings, loaded with either 4µg model small molecule or 400µg dextran (**Fig. 6A-C**) or drop-cast to make free-standing films (3mm diameter) (**Fig. 6D-F**) as previously described. All coatings were incubated in 1mL PBS for the first 14 days, with daily sampling and full buffer replacement. After 14 days, the C6-loaded coatings were switched to a PBS + 0.1% Triton X-100 buffer to enhance solubility, while the dextran-loaded coatings were changed into a solution of PBS + 80µM H_2O_2 for 7d and then finally PBS + 320µM H_2O_2 for the final 7d (all with daily sampling and full buffer replacement). All films were incubated in 250µL of release buffer (PBS, PBS + 80µM H_2O_2, PBS + 800µM H_2O_2) and sampled daily with full buffer replacement. For pulsed H_2O_2 experiments, HEC_{MTP} films were exposed to 24-hour pulses of 800µM H_2O_2 after 2, 5, and 8 days of incubation in PBS-only solutions. All collected samples were read on a Molecular Devices SpectraMax i3X Microplate Detection Platform using an Excitation/Emission appropriate for each molecule (C1 (375/445nm); C6 (443/505nm); 4MU (360/450nm); FITC-dextran polymers (491/516nm))

Neural Progenitor Cell (NPC) Culture and Differentiation
NPCs were cultured as previously described (*94*, *95*). Briefly, the cells were grown in neural expansion (NE) media consisting of DMEM/F12 supplemented with B27 and growth factors EGF and FGF (100 ng/mL for each). NPC stocks were maintained so that all cell stocks used in this study were less than P30. For astrocyte differentiation, NE media was removed and replaced with astrocyte differentiation media consisting of DMEM/F12 supplemented with B27 and 1% fetal bovine serum (FBS) for 72hrs.

Cytotoxicity Assay and Non-fouling Assay
A 96-well plate was coated with 75µL 1wt% HEC, HEC_{MTP}, HEC_{HEX} in DMSO for 1 hour at 35°C. The solution was removed, and well plates were dried in a vacuum oven as previously described. After drying, wells were treated with H_2O_2 as appropriate, and all wells were washed once with PBS before UV sterilization.

Following differentiation, astrocytes were trypsinized, resuspended in differentiation media, plated onto the well plates at 50k cells/well, and allowed to adhere for 24hrs (original plate). After 24hrs, the supernatant was collected for all wells and added to a separate, tissue culture-treated well plate (transfer plate). The cells were allowed to adhere for 24hrs before testing the viability and fouling. For the dead control, an 80% methanol solution was added to the cells and allowed to incubate for 30min. A fresh stock of Calcein AM solution was prepared at a molarity of 2µM. 100µL of Calcein AM was added to each well and allowed to incubate for 30min. The 96-well plate was read on a Molecular Devices SpectraMax i3X Microplate Detection Platform using an Excitation/Emission of 488/520nm. Viability was determined as the sum of the original plate and the transfer plate, with the results normalized to the live/dead columns where the HEC column represents 100% viability and dead represents 0% viability. Fouling percent was determined as the ratio of Calcein AM signal in the original plate over the sum of the signal from the two plates.

Protein Fouling Assay
HEC_{MTP} films were created as previously described. HEC_{MTP} films were then punched out using a 1mm diameter biopsy punch and placed into PBS +/- 800µM H_2O_2 for 24 hours. HEC_{MTP} films were then transferred into PBS for an additional 24 hours. Gelatin hydrogels were formed by solubilizing gelatin at 50 mg/mL in PBS while heating in a water bath at 85°C. Soluble gelatin was deposited into a silicone mold (3mm diameter) and allowed to cool for 24hrs. Subsequently, gelatin gels were removed from the silicone mold and transferred into PBS for 24 hours. To test protein fouling, hydrated HEC_{MTP} films (+/- 800µM H_2O_2) and gelatin were placed in 1mL of 0.5mg/mL albumin-fluorescein isothiocyanate conjugate (FITC-BSA) solubilized in PBS for 1hr. After 1hr, samples were transferred onto a coverslip and imaged with an Olympus IX83 epifluorescent microscope. Images were taken at a standardized exposure time and evaluated using a standard intensity setting. Mean fluorescence intensity was measured within a 500x500µm area at the center of the materials using NIH Image J (1.53) software.

Biomaterial Implant Formation
To prepare sterile films for implantation, HEC_{MTP}, HEC_{HEX}, and HEC_{OCT} stocks were first sterile filtered as 1wt% solutions in DMSO and subsequently dialyzed against MilliQ water and lyophilized under minimal particulate conditions. HEC_{MTP}, HEC_{HEX}, and HEC_{OCT} films were then fabricated as previously described. Layering and drying steps were repeated to form films of thickness 100-200µm. Regenerated cellulose (RC) implants were formed from 1kDa RC dialysis bags (Spectrum, P/N: 132104). These materials were dialyzed and lyophilized under the same conditions to form a dry film. Individual subcutaneous implants were then punched from these films using a 3mm biopsy punch. Subcutaneous implants were autoclaved and stored sterile until implantation. Prior to implantation, subcutaneous implants were hydrated in sterile PBS for 24hrs (HEC_{MTP}, RC) or at the time of surgery (HEC_{HEX}, HEC_{OCT}).

Subcutaneous Implant Surgery
All surgical procedures were approved by the BU IACUC (Protocol number: PROTO202100013) and conducted within a designated surgical facility. All procedures were performed on mice C57/BL6 female mice (Cat#000664, JAX) that were aged 8–12 weeks at the time of surgery under general anesthesia achieved through inhalation of isoflurane in oxygen-enriched air. The dorsal regions of the mice were shaved, stabilized, and horizontally leveled using a stereotaxic apparatus with ear bars (David Kopf, Tujunga, CA, USA) and a custom device to hold the mouse tail taut. A small incision was made on the dorsum and the subcutaneous tissue was separated from muscle via blunt dissection. Placement of hydrated subcutaneous implants (HEC_{MTP}, HEC_{HEX}, HEC_{OCT}, and RC) was visually aided by an operating microscope, with each mouse receiving 4 implants (2 per side). After placement of subcutaneous implants, the surgical incision site was sutured closed, and the animals were allowed to recover.

Transcardial Perfusions
After terminal anesthesia by an overdose of isoflurane, mice were perfused transcardially with heparinized saline (10 units mL^{-1} of heparin) and 4% paraformaldehyde (PFA) that was freshly prepared from 32% PFA aqueous solution (Cat# 15 714, EMS), using a peristaltic pump at a rate of 7 mL min^{-1}. Approximately 10 mL of heparinized saline and 50 mL of 4% PFA were used per animal. Following perfusion, the skin (epidermis, dermis, subcutaneous) was resected, and the 4 subcutaneous implants were located. This tissue was placed in 4% PFA for 48 hours, then transferred into 0.01% sodium azide in Tris-buffered saline (TBS) for at least 3d with the replacement after 2d and stored at 4 °C until further use.

Histological Staining, Brightfield Imaging, and Image Analysis
Tissue samples were embedded, cut, and stained with hematoxylin and eosin (H&E), as well as Masson's Trichrome (MT) by the Tufts Animal Histology Core. All histological images were taken using an Olympus Virtual Slide Microscope (VS120). Quantification of peri-implant, fibrotic capsule thickness (defined as all collagenous tissue below the PC muscle layer) and dense collagen capsule thickness (defined by intensity of MT stain and fiber morphology at implant surface) was performed using NIH Image J (1.53) software. Dense collagen capsule thickness was calculated by dividing the measured dense collagen area by the average of the outer and inner perimeters. Missing or defective portions of the capsule were excluded. Morphology-based classification of cells immediately adjacent to biomaterial implant was performed using the QuPath software (*96*). Fibroblasts were defined as cells with elongated nuclei whereas round or irregular cells were classified as macrophages. Large, multinucleated cells were classified as foreign body giant cells (FBGCs) and cells with lobed nuclei were defined as neutrophils. Due to relative sparsity, FBGCs and neutrophils were excluded from further analysis. Cellular densities were obtained by counting the number of cells within 20 µm of each implant (tissue sections were 5µm thick).

Statistical Analysis
Graph generation and statistical evaluations of repeated measures were conducted by one-way or two-way ANOVA with post hoc independent pairwise analysis via Tukey's multiple comparison test or by Student's t-tests where appropriate using Prism 10 (GraphPad Software Inc, San Diego, CA). Statistical details of experiments can be found in the figure legends, including the statistical tests used and the number of replicate samples. Across all statistical tests, significance was defined as p-value <0.05. Unless

otherwise specified, all graphs show mean values plus or minus standard error of the means (s.e.m.) as well as individual values overlaid as dot plots.

References

1. R. S. Sanders, M. T. Lee, Implantable pacemakers. *Proceedings of the IEEE* **84**, 480–486 (1996).
2. L. Almadrones, P. Campana, E. C. Dantis, Arterial, peritoneal, and intraventricular access devices. *Seminars in Oncology Nursing* **11**, 194–202 (1995).
3. D. D. Dougherty, Deep Brain Stimulation: Clinical Applications. *Psychiatric Clinics of North America* **41**, 385–394 (2018).
4. S. Belverud, A. Mogilner, M. Schulder, Intrathecal pumps. *Neurotherapeutics* **5**, 114–122 (2008).
5. J. S. Siopack, H. E. Jergesen, Total hip arthroplasty. *West J Med* **162**, 243–249 (1995).
6. M. Abdul-Al, A. Zaernia, F. Sefat, Biomaterials for breast reconstruction: Promises, advances, and challenges. *Journal of Tissue Engineering and Regenerative Medicine* **14**, 1549–1569 (2020).
7. W. Khan, E. Muntimadugu, M. Jaffe, A. J. Domb, "Implantable Medical Devices" in *Focal Controlled Drug Delivery*, A. J. Domb, W. Khan, Eds. (Springer US, Boston, MA, 2014; https://doi.org/10.1007/978-1-4614-9434-8_2), pp. 33–59.
8. M. Pinget, N. Jeandidier, Long Term Safety and Efficacy of Intraperitoneal Insulin Infusion by Means of Implantable Pumps. *Horm Metab Res* **30**, 475–486 (1998).
9. J. Craik, S. Rowlands, "Contraceptive Devices for Women: Implants, Intrauterine Devices and Other Products" in *Medicines For Women*, M. Harrison-Woolrych, Ed. (Springer International Publishing, Cham, 2015; https://doi.org/10.1007/978-3-319-12406-3_8), pp. 227–270.
10. K. Junge, M. Binnebösel, K. T. von Trotha, R. Rosch, U. Klinge, U. P. Neumann, P. Lynen Jansen, Mesh biocompatibility: effects of cellular inflammation and tissue remodelling. *Langenbecks Arch Surg* **397**, 255–270 (2012).
11. M. K. Harman, "3.1.9 - Medical Device Failure—Implant Retrieval, Evaluation, and Failure Analysis" in *Biomaterials Science (Fourth Edition)*, W. R. Wagner, S. E. Sakiyama-Elbert, G. Zhang, M. J. Yaszemski, Eds. (Academic Press, 2020; https://www.sciencedirect.com/science/article/pii/B9780128161371000969), pp. 1485–1495.
12. V. K. Vendra, L. Wu, S. Krishnan, "Polymer Thin Films for Biomedical Applications" in *Nanotechnologies for the Life Sciences* (John Wiley & Sons, Ltd, 2011; https://onlinelibrary.wiley.com/doi/abs/10.1002/9783527610419.ntls0179).
13. H. Zhang, M. Chiao, Anti-fouling Coatings of Poly(dimethylsiloxane) Devices for Biological and Biomedical Applications. *J. Med. Biol. Eng.* **35**, 143–155 (2015).
14. S. Jon, J. Seong, A. Khademhosseini, T.-N. T. Tran, P. E. Laibinis, R. Langer, Construction of Nonbiofouling Surfaces by Polymeric Self-Assembled Monolayers. *Langmuir* **19**, 9989–9993 (2003).
15. K. Jayakumar, A. Lielpetere, D. A. Domingo-Lopez, R. E. Levey, G. P. Duffy, W. Schuhmann, D. Leech, Tethering zwitterionic polymer coatings to mediated glucose biosensor enzyme electrodes can decrease sensor foreign body response yet retain sensor sensitivity to glucose. *Biosensors and Bioelectronics* **219**, 114815 (2023).
16. L. Zhang, Z. Cao, T. Bai, L. Carr, J.-R. Ella-Menye, C. Irvin, B. D. Ratner, S. Jiang, Zwitterionic hydrogels implanted in mice resist the foreign-body reaction. *Nat Biotechnol* **31**, 553–556 (2013).
17. D. Chan, C. L. Maikawa, A. I. d'Aquino, S. S. Raghavan, M. L. Troxell, E. A. Appel, Polyacrylamide-based hydrogel coatings improve biocompatibility of implanted pump devices. *Journal of Biomedical Materials Research Part A* **111**, 910–920 (2023).
18. C. Zhao, J. Zheng, Synthesis and Characterization of Poly(N-hydroxyethylacrylamide) for Long-Term Antifouling Ability. *Biomacromolecules* **12**, 4071–4079 (2011).
19. S. Capuani, G. Malgir, C. Y. X. Chua, A. Grattoni, Advanced strategies to thwart foreign body response to implantable devices. *Bioengineering & Translational Medicine* **7**, e10300 (2022).
20. D. Zhang, Q. Chen, C. Shi, M. Chen, K. Ma, J. Wan, R. Liu, Dealing with the Foreign-Body Response to Implanted Biomaterials: Strategies and Applications of New Materials. *Advanced Functional Materials* **31**, 2007226 (2021).
21. M. Ferguson, D. Sharma, D. Ross, F. Zhao, A Critical Review of Microelectrode Arrays and Strategies for Improving Neural Interfaces. *Advanced Healthcare Materials* **8**, 1900558 (2019).
22. X. Zhou, Y. Wang, J. Ji, P. Zhang, Materials Strategies to Overcome the Foreign Body Response. *Advanced Healthcare Materials* **n/a**, 2304478.
23. C. Skjöldebrand, J. L. Tipper, P. Hatto, M. Bryant, R. M. Hall, C. Persson, Current status and future potential of wear-resistant coatings and articulating surfaces for hip and knee implants. *Materials Today Bio* **15**, 100270 (2022).
24. Q. Wei, X. Liu, Q. Yue, S. Ma, F. Zhou, Mussel-Inspired One-Step Fabrication of Ultralow-Friction Coatings on Diverse Biomaterial Surfaces. *Langmuir* **35**, 8068–8075 (2019).

25. K. C. Spencer, J. C. Sy, K. B. Ramadi, A. M. Graybiel, R. Langer, M. J. Cima, Characterization of Mechanically Matched Hydrogel Coatings to Improve the Biocompatibility of Neural Implants. *Sci Rep* **7**, 1952 (2017).
26. M. F. Montemor, Functional and smart coatings for corrosion protection: A review of recent advances. *Surface and Coatings Technology* **258**, 17–37 (2014).
27. S. Rammelt, T. Illert, S. Bierbaum, D. Scharnweber, H. Zwipp, W. Schneiders, Coating of titanium implants with collagen, RGD peptide and chondroitin sulfate. *Biomaterials* **27**, 5561–5571 (2006).
28. H. Yan, C. Seignez, M. Hjorth, B. Winkeljann, M. Blakeley, O. Lieleg, M. Phillipson, T. Crouzier, Immune-Informed Mucin Hydrogels Evade Fibrotic Foreign Body Response In Vivo. *Advanced Functional Materials* **29**, 1902581 (2019).
29. M. T. Wolf, C. A. Carruthers, C. L. Dearth, P. M. Crapo, A. Huber, O. A. Burnsed, R. Londono, S. A. Johnson, K. A. Daly, E. C. Stahl, J. M. Freund, C. J. Medberry, L. E. Carey, A. Nieponice, N. J. Amoroso, S. F. Badylak, Polypropylene surgical mesh coated with extracellular matrix mitigates the host foreign body response. *Journal of Biomedical Materials Research Part A* **102**, 234–246 (2014).
30. H. C. Tan, C. K. Poh, Y. Cai, W. Wang, Anti-fibrosis effect of BMP-7 peptide functionalization on cobalt chromium alloy. *Journal of Orthopaedic Research* **31**, 983–990 (2013).
31. R. P. Tan, N. Hallahan, E. Kosobrodova, P. L. Michael, F. Wei, M. Santos, Y. T. Lam, A. H. P. Chan, Y. Xiao, M. M. M. Bilek, P. Thorn, S. G. Wise, Bioactivation of Encapsulation Membranes Reduces Fibrosis and Enhances Cell Survival. *ACS Appl. Mater. Interfaces* **12**, 56908–56923 (2020).
32. Y. Lu, D. Wang, T. Li, X. Zhao, Y. Cao, H. Yang, Y. Y. Duan, Poly(vinyl alcohol)/poly(acrylic acid) hydrogel coatings for improving electrode–neural tissue interface. *Biomaterials* **30**, 4143–4151 (2009).
33. M. Yao, Z. Wei, J. Li, Z. Guo, Z. Yan, X. Sun, Q. Yu, X. Wu, C. Yu, F. Yao, S. Feng, H. Zhang, J. Li, Microgel reinforced zwitterionic hydrogel coating for blood-contacting biomedical devices. *Nat Commun* **13**, 5339 (2022).
34. W. Feng, Z. Wang, Tailoring the Swelling-Shrinkable Behavior of Hydrogels for Biomedical Applications. *Advanced Science* **10**, 2303326 (2023).
35. M. Shur, O. Akouissi, O. Rizzo, D. J. Colin, J. M. Kolinski, S. P. Lacour, Revealing the complexity of ultra-soft hydrogel re-swelling inside the brain. *Biomaterials* **294**, 122024 (2023).
36. R. I. Mehta, R. I. Mehta, Hydrophilic Polymer Embolism: An Update for Physicians. *The American Journal of Medicine* **130**, e287–e290 (2017).
37. S. R. Meyers, M. W. Grinstaff, Biocompatible and bioactive surface modifications for prolonged in vivo efficacy. *Chem Rev* **112**, 10.1021/cr2000916 (2012).
38. X. Li, X. Liu, B. Josey, C. J. Chou, Y. Tan, N. Zhang, X. Wen, Short Laminin Peptide for Improved Neural Stem Cell Growth. *Stem Cells Transl Med* **3**, 662–670 (2014).
39. S. Bhatia, "Natural Polymers vs Synthetic Polymer" in *Natural Polymer Drug Delivery Systems: Nanoparticles, Plants, and Algae*, S. Bhatia, Ed. (Springer International Publishing, Cham, 2016; https://doi.org/10.1007/978-3-319-41129-3_3), pp. 95–118.
40. S. R. Caliari, J. A. Burdick, A practical guide to hydrogels for cell culture. *Nat Methods* **13**, 405–414 (2016).
41. R. Sanz-Horta, A. Matesanz, A. Gallardo, H. Reinecke, J. L. Jorcano, P. Acedo, D. Velasco, C. Elvira, Technological advances in fibrin for tissue engineering. *J Tissue Eng* **14**, 20417314231190288 (2023).
42. D. R. Wiggam, W. E. Gloor, Lacquer Development during 100 Years. *Ind. Eng. Chem.* **26**, 551–553 (1934).
43. J. Vienken, Polymers in Nephrology Characteristics and Needs. *Int J Artif Organs* **25**, 470–479 (2002).
44. K. J. Edgar, Cellulose esters in drug delivery. *Cellulose* **14**, 49–64 (2007).
45. E. A. Carter, B. Swarbrick, T. M. Harrison, L. Ronai, Rapid identification of cellulose nitrate and cellulose acetate film in historic photograph collections. *Heritage Science* **8**, 51 (2020).
46. C. J. Malm, H. L. Smith, Properties of Lacquer-Type Cellulose Acetate Butyrates. *Ind. Eng. Chem.* **41**, 2325–2334 (1949).
47. S. Smith, *The Cellulose Lacquers: A Practical Handbook on Their Manufacture* (Sir I. Pitman & sons, Limited, 1928).
48. W. E. Gloor, Durability of Cellulose Mixed-Ester Lacquers. *Ind. Eng. Chem.* **29**, 690–696 (1937).
49. C. R. Fordyce, M. Salo, G. R. Clarke, Cellulose Mixed-Ester Lacquers. *Ind. Eng. Chem.* **28**, 1310–1313 (1936).
50. American Chemical Society National Historic Chemical Landmarks. Scotch® Transparent Tape, *American Chemical Society*. https://www.acs.org/education/whatischemistry/landmarks/scotchtape.html.
51. T. Heinze, "Cellulose: Structure and Properties" in *Cellulose Chemistry and Properties: Fibers, Nanocelluloses and Advanced Materials*, O. J. Rojas, Ed. (Springer International Publishing, Cham, 2016; https://doi.org/10.1007/12_2015_319), pp. 1–52.
52. J.-L. Wertz, O. Bédué, J. P. Mercier, *Cellulose Science and Technology* (EPFL Press, 2010).
53. H. Seddiqi, E. Oliaei, H. Honarkar, J. Jin, L. C. Geonzon, R. G. Bacabac, J. Klein-Nulend, Cellulose and its derivatives: towards biomedical applications. *Cellulose* **28**, 1893–1931 (2021).
54. A. R. Pascual, M. E. E. Martín, *Cellulose* (2019; https://www.intechopen.com/books/7363).

55. K. J. Edgar, C. M. Buchanan, J. S. Debenham, P. A. Rundquist, B. D. Seiler, M. C. Shelton, D. Tindall, Advances in cellulose ester performance and application. *Progress in Polymer Science* **26**, 1605–1688 (2001).
56. L.-C. Xu, C. A. Siedlecki, Effects of surface wettability and contact time on protein adhesion to biomaterial surfaces. *Biomaterials* **28**, 3273–3283 (2007).
57. G. Zhou, H. Loppnow, T. Groth, A macrophage/fibroblast co-culture system using a cell migration chamber to study inflammatory effects of biomaterials. *Acta Biomaterialia* **26**, 54–63 (2015).
58. Y. Tabata, Y. Ikada, Effect of surface wettability of microspheres on phagocytosis. *Journal of Colloid and Interface Science* **127**, 132–140 (1989).
59. T. J. Deming, Functional Modification of Thioether Groups in Peptides, Polypeptides, and Proteins. *Bioconjugate Chem.* **28**, 691–700 (2017).
60. A. L. Wollenberg, T. M. O'Shea, J. H. Kim, A. Czechanski, L. G. Reinholdt, M. V. Sofroniew, T. J. Deming, Injectable polypeptide hydrogels via methionine modification for neural stem cell delivery. *Biomaterials* **178**, 527–545 (2018).
61. Z. Wang, J. Yao, M. Bavcon Kralj, D. Dolenc, P. Trebše, Removal of Flotation Collector O-Isopropyl-N-ethylthionocarbamate from Wastewater. *Molecules* **26**, 6676 (2021).
62. T. Tarantelli, C. Furlani, Palladium(II) and platinum(II) complexes of thiocarbamic esters. *J. Chem. Soc. A*, 1213–1217 (1971).
63. N. Mozhzhukhina, L. P. Méndez De Leo, E. J. Calvo, Infrared Spectroscopy Studies on Stability of Dimethyl Sulfoxide for Application in a Li–Air Battery. *J. Phys. Chem. C* **117**, 18375–18380 (2013).
64. J. M. Sarapas, G. N. Tew, Poly(ether–thioethers) by Thiol–Ene Click and Their Oxidized Analogues as Lithium Polymer Electrolytes. *Macromolecules* **49**, 1154–1162 (2016).
65. A. J. van der Vlies, J. Xu, M. Ghasemi, C. Bator, A. Bell, B. Rosoff-Verbit, B. Liu, E. D. Gomez, U. Hasegawa, Thioether-Based Polymeric Micelles with Fine-Tuned Oxidation Sensitivities for Chemotherapeutic Drug Delivery. *Biomacromolecules* **23**, 77–88 (2022).
66. F. E. Bartell, B. R. Ray, Wetting Characteristics of Cellulose Derivatives. I. Contact Angles Formed by Water and by Organic Liquids. *J. Am. Chem. Soc.* **74**, 778–783 (1952).
67. C. J. Brinker, "Dip Coating" in *Chemical Solution Deposition of Functional Oxide Thin Films*, T. Schneller, R. Waser, M. Kosec, D. Payne, Eds. (Springer, Vienna, 2013; https://doi.org/10.1007/978-3-211-99311-8_10), pp. 233–261.
68. D. Grosso, How to exploit the full potential of the dip-coating process to better control film formation. *Journal of Materials Chemistry* **21**, 17033–17038 (2011).
69. S. L. Patil, S. R. Sankapal, F. M. A. Almuntaser, "Dip Coating: Simple Way of Coating Thin Films" in *Simple Chemical Methods for Thin Film Deposition: Synthesis and Applications*, B. R. Sankapal, A. Ennaoui, R. B. Gupta, C. D. Lokhande, Eds. (Springer Nature, Singapore, 2023; https://doi.org/10.1007/978-981-99-0961-2_10), pp. 425–447.
70. F. El-Mohtadi, R. d'Arcy, N. Tirelli, Oxidation-Responsive Materials: Biological Rationale, State of the Art, Multiple Responsiveness, and Open Issues. *Macromolecular Rapid Communications* **40**, 1800699 (2019).
71. P. A. Hyslop, Z. Zhang, D. V. Pearson, L. A. Phebus, Measurement of striatal H2O2 by microdialysis following global forebrain ischemia and reperfusion in the rat: correlation with the cytotoxic potential of H2O2 in vitro. *Brain Research* **671**, 181–186 (1995).
72. T. D. Chung, R. M. Linville, Z. Guo, R. Ye, R. Jha, G. N. Grifno, P. C. Searson, Effects of acute and chronic oxidative stress on the blood–brain barrier in 2D and 3D in vitro models. *Fluids Barriers CNS* **19**, 33 (2022).
73. S. Dumitriu, *Polysaccharides: Structural Diversity and Functional Versatility, Second Edition* (CRC Press, 2004).
74. J.-H. Shin, T. Kondo, Cellulosic blends with poly(acrylonitrile): characterization of hydrogen bonds using regioselectively methylated cellulose derivatives. *Polymer* **39**, 6899–6904 (1998).
75. W. J. Middleton, R. V. Lindsey, Hydrogen Bonding in Fluoro Alcohols. *J. Am. Chem. Soc.* **86**, 4948–4952 (1964).
76. I. Colomer, A. E. R. Chamberlain, M. B. Haughey, T. J. Donohoe, Hexafluoroisopropanol as a highly versatile solvent. *Nat Rev Chem* **1**, 1–12 (2017).
77. S. P. Lacour, G. Courtine, J. Guck, Materials and technologies for soft implantable neuroprostheses. *Nat Rev Mater* **1**, 1–14 (2016).
78. A. M. Villarreal-Gómez, R. Torregrosa-Coque, J. M. Martín-Martínez, "Comparative Properties of Ethyl, n-Butyl, and n-Octyl Cyanoacrylate Bioadhesives Intended for Wound Closure" in *Biologically Responsive Biomaterials for Tissue Engineering*, I. Antoniac, Ed. (Springer, New York, NY, 2013; https://doi.org/10.1007/978-1-4614-4328-5_5), pp. 89–106.
79. Q. Yang, A. L. Vazquez, X. T. Cui, Long-term in vivo two-photon imaging of the neuroinflammatory response to intracortical implants and micro-vessel disruptions in awake mice. *Biomaterials* **276**, 121060 (2021).
80. K. De, V. Masilamani, Image Sharpness Measure for Blurred Images in Frequency Domain. *Procedia Engineering* **64**, 149–158 (2013).
81. A. Napoli, M. Valentini, N. Tirelli, M. Müller, J. A. Hubbell, Oxidation-responsive polymeric vesicles. *Nature*

Mater **3**, 183–189 (2004).
82. T. M. O'Shea, A. L. Wollenberg, J. H. Kim, Y. Ao, T. J. Deming, M. V. Sofroniew, Foreign body responses in central nervous system mimic natural wound responses and alter biomaterial functions, *Nature Communications*. **11** (2020). https://doi.org/10.1038/s41467-020-19906-3.
83. A. R. Adamantidis, F. Zhang, A. M. Aravanis, K. Deisseroth, L. de Lecea, Neural substrates of awakening probed with optogenetic control of hypocretin neurons. *Nature* **450**, 420–424 (2007).
84. D. Aharoni, B. S. Khakh, A. J. Silva, P. Golshani, All the light that we can see: a new era in miniaturized microscopy. *Nat Methods* **16**, 11–13 (2019).
85. T. H. Chia, M. J. Levene, Microprisms for In Vivo Multilayer Cortical Imaging. *Journal of Neurophysiology* **102**, 1310–1314 (2009).
86. T. Kushibiki, "Current Topics of Optogenetics for Medical Applications Toward Therapy" in *Optogenetics: Light-Sensing Proteins and Their Applications in Neuroscience and Beyond*, H. Yawo, H. Kandori, A. Koizumi, R. Kageyama, Eds. (Springer Singapore, Singapore, 2021; https://doi.org/10.1007/978-981-15-8763-4_35), pp. 513–521.
87. F. Chu, G. Zhao, W. Li, W. Wei, W. Chen, Z. Ma, Z. Gao, N. S. Shuaibu, J. Luo, B. Yu, H. Feng, Y. Pan, X. Wang, Catalyst-Free Oxidation Reactions in a Microwave Plasma Torch-Based Ion/Molecular Reactor: An Approach for Predicting the Atmospheric Oxidation of Pollutants. *Anal. Chem.* **95**, 2004–2010 (2023).
88. A. Mantovani, M. A. Cassatella, C. Costantini, S. Jaillon, Neutrophils in the activation and regulation of innate and adaptive immunity. *Nat Rev Immunol* **11**, 519–531 (2011).
89. S. Jhunjhunwala, Neutrophils at the Biological–Material Interface. *ACS Biomater. Sci. Eng.* **4**, 1128–1136 (2018).
90. J. O. Abaricia, A. H. Shah, R. M. Musselman, R. Olivares-Navarrete, Hydrophilic titanium surfaces reduce neutrophil inflammatory response and NETosis. *Biomater. Sci.* **8**, 2289–2299 (2020).
91. J. Liu, X. Han, T. Zhang, K. Tian, Z. Li, F. Luo, Reactive oxygen species (ROS) scavenging biomaterials for anti-inflammatory diseases: from mechanism to therapy. *J Hematol Oncol* **16**, 116 (2023).
92. S. J. Nelson, J. J. Creechley, M. E. Wale, T. J. Lujan, Print-A-Punch: A 3D printed device to cut dumbbell-shaped specimens from soft tissue for tensile testing. *J Biomech* **112**, 110011 (2020).
93. E. M. DuBois, H. O. Adewumi, P. R. O'Connor, J. E. Labovitz, T. M. O'Shea, Trehalose-Guanosine Glycopolymer Hydrogels Direct Adaptive Glia Responses in CNS Injury. *Advanced Materials* **35**, 2211774 (2023).
94. T. M. O'Shea, Y. Ao, S. Wang, A. L. Wollenberg, J. H. Kim, R. A. Ramos Espinoza, A. Czechanski, L. G. Reinholdt, T. J. Deming, M. V. Sofroniew, Lesion environments direct transplanted neural progenitors towards a wound repair astroglial phenotype in mice. *Nat Commun* **13**, 5702 (2022).
95. H. O. Adewumi, G. I. Berniac, E. A. McCarthy, T. M. O'Shea, Ischemic and hemorrhagic stroke lesion environments differentially alter the glia repair potential of neural progenitor cell and immature astrocyte grafts. *Experimental Neurology* **374**, 114692 (2024).
96. P. Bankhead, M. B. Loughrey, J. A. Fernández, Y. Dombrowski, D. G. McArt, P. D. Dunne, S. McQuaid, R. T. Gray, L. J. Murray, H. G. Coleman, J. A. James, M. Salto-Tellez, P. W. Hamilton, QuPath: Open source software for digital pathology image analysis. *Sci Rep* **7**, 16878 (2017).

Acknowledgments

This research was supported by the Biomedical Engineering Core Facilities at Boston University (BU). A special thanks to Xin Brown and the Biointerface Technologies (BIT) core, as well as the Micro and Nano Imaging (MNI) core at BU. This research was also supported by the BU Chemistry Department Chemical Instrumentation Center and staff. We thank the Boston University Neurophotonics center for providing the Bruker Ultima Investigator two-photon microscope used in this work. We are grateful to the National Science Foundation for the purchase of the NMR's (CHE0619339) and PHI Genesis XPS system (CHE-2216008) used in this work. We also thank the Boston University Micro and Nano Imaging Facility and the Office of the Director, National Institutes of Health for their support under Award Number S10OD024993 (this content is solely the responsibility of the authors and does not reflect the official views of the NIH). We thank Lu Ping for help with XPS, Cara Ravasio for many helpful discussions, and both Patrick Kulaga and Jacob Labovitz for time spent on histological analysis. We also thank the Tufts Animal Histology Core for their processing and staining of the tissue.

Funding:
Internal Boston University start-up funds, Boston University (TMO)
Deans Catalyst Award, College of Engineering, Boston University (TMO)

Author contributions:

Conceptualization: TMO, EMD
Methodology: EMD, KEH, MGS, LFH, RS, PRO
Validation: EMD, KEH, MGS
Formal Analysis: EMD, KEH, MGS
Investigation: EMD, KEH, MGS, LFH, RS, PRO, TMO
Writing—original draft: EMD, KEH, MGS, TMO
Writing—review & editing: EMD, KEH, MGS, LFH, RS, PRO, TMO
Visualization: EMD, KEH, MGS
Supervision: EMD, KEH, MGS, TMO
Project Administration: EMD, TMO
Funding Acquisition: TMO

Competing interests: Authors declare that they have no competing interests. A patent application describing the polymer technology has been submitted.

Data and materials availability: All data needed to evaluate the conclusions in the paper are present in the paper and/or the Supplementary Materials. Materials can be made available upon request.

Supplementary Materials